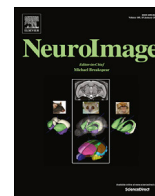




Contents lists available at ScienceDirect

NeuroImage

journal homepage: www.elsevier.com/locate/neuroimage

Inherent physiological artifacts in EEG during tDCS

Nigel Gebodh^{a,**}, Zeinab Esmailpour^a, Devin Adair^b, Kenneth Chelette^c, Jacek Dmochowski^a, Adam J. Woods^d, Emily S. Kappenman^e, Lucas C. Parra^a, Marom Bikson^{a,b,*}

^a Neural Engineering Laboratory, Department of Biomedical Engineering, The City College of New York of the City University of New York, New York, NY, USA

^b Department of Psychology, The Graduate Center at City University of New York, New York, NY, USA

^c ANT Neuro North America, Madison, WI, USA

^d Center for Cognitive Aging and Memory, McKnight Brain Institute, Department of Clinical and Health Psychology, Department of Neuroscience, University of Florida, Gainesville, FL, USA

^e San Diego State University, San Diego, CA, USA



ARTICLE INFO

Keywords:

Electroencephalography (EEG)
Transcranial direct current stimulation (tDCS)
Transcranial electric stimulation (tES)
Physiological artifact
Finite element method (FEM)
Electrocardiogram (ECG)

ABSTRACT

Online imaging and neuromodulation is invalid if stimulation distorts measurements beyond the point of accurate measurement. In theory, combining transcranial Direct Current Stimulation (tDCS) with electroencephalography (EEG) is compelling, as both use non-invasive electrodes and image-guided dose can be informed by the reciprocity principle. To distinguish real changes in EEG from stimulation artifacts, prior studies applied conventional signal processing techniques (e.g. high-pass filtering, ICA). Here, we address the assumptions underlying the suitability of these approaches. We distinguish *physiological artifacts* - defined as artifacts resulting from interactions between the stimulation induced voltage and the body and so inherent regardless of tDCS or EEG hardware performance - from *methodology-related artifacts* - arising from non-ideal experimental conditions or non-ideal stimulation and recording equipment performance. Critically, we identify *inherent physiological artifacts* which are present in all online EEG-tDCS: 1) cardiac distortion and 2) ocular motor distortion. In conjunction, *non-inherent physiological artifacts* which can be minimized in most experimental conditions include: 1) motion and 2) myogenic distortion. Artifact dynamics were analyzed for varying stimulation parameters (montage, polarity, current) and stimulation hardware. Together with concurrent physiological monitoring (ECG, respiration, ocular, EMG, head motion), and current flow modeling, each physiological artifact was explained by biological source-specific body impedance changes, leading to incremental changes in scalp DC voltage that are significantly larger than real neural signals. Because these artifacts modulate the DC voltage and scale with applied current, they are dose specific such that their contamination cannot be accounted for by conventional experimental controls (e.g. differing stimulation montage or current as a control). Moreover, because the EEG artifacts introduced by physiologic processes during tDCS are high dimensional (as indicated by Generalized Singular Value Decomposition- GSVD), non-stationary, and overlap highly with neurogenic frequencies, these artifacts cannot be easily removed with conventional signal processing techniques. Spatial filtering techniques (GSVD) suggest that the removal of physiological artifacts would significantly degrade signal integrity. Physiological artifacts, as defined here, would emerge only during tDCS, thus processing techniques typically applied to EEG in the absence of tDCS would not be suitable for artifact removal during tDCS. All concurrent EEG-tDCS must account for physiological artifacts that are a) present regardless of equipment used, and b) broadband and confound a broad range of experiments (e.g. oscillatory activity and event related potentials). Removal of these artifacts requires the recognition of their non-stationary, physiology-specific dynamics, and individualized nature. We present a broad taxonomy of artifacts (non/stimulation related), and suggest possible approaches and challenges to denoising online EEG-tDCS stimulation artifacts.

* Corresponding author. Center for Discovery and Innovation (CDI), 85 St Nicholas Terrace, New York, NY 10031, USA.

** Corresponding author. Center for Discovery and Innovation (CDI), 85 St Nicholas Terrace, New York, NY 10031, USA.

E-mail addresses: ngebodh01@citymail.cuny.edu (N. Gebodh), zesmaeilpour@ccny.cuny.edu (Z. Esmailpour), dadair@gradcenter.cuny.edu (D. Adair), jdmochowski@ccny.cuny.edu (J. Dmochowski), ajwoods@phhp.ufl.edu (A.J. Woods), emily.kappenman@sdsu.edu (E.S. Kappenman), parra@ccny.cuny.edu (L.C. Parra), bikson@ccny.cuny.edu (M. Bikson).

<https://doi.org/10.1016/j.neuroimage.2018.10.025>

Received 16 May 2018; Received in revised form 10 September 2018; Accepted 8 October 2018

Available online 12 October 2018

1053-8119/© 2018 Elsevier Inc. All rights reserved.

1. Introduction

The integration of non-invasive brain stimulation with imaging, particularly concurrent (online) integration, provides objective outcome measures and allows for the optimization of interventions (Baudewig et al., 2001; Charvet et al., 2015; Hunter et al., 2013; Komssi et al., 2002). In order for these combined modalities to be informative, stimulation induced artifacts during concurrent stimulation and signal acquisition need to be addressed (Antal et al., 2014; Baudewig et al., 2018; Chung et al., 2015; Garcia-Cossio et al., 2016). Both electroencephalography (EEG) and High Definition transcranial Direct Current Stimulation (HD-tDCS; Minhas et al., 2010) use gel interfaces between electrodes and the scalp, across the head, are portable and low-cost (Charvet et al., 2015; Greischar et al., 2004), and have broad applications spanning cognitive and neuropsychiatric domains (Al-Kaysi et al., 2017; Brunoni et al., 2012; Buch et al., 2017; Castillo-Saavedra et al., 2016); making them compatible modalities for studying how stimulation changes brain activity online. In addition, the concept of reciprocity, when applied to EEG and transcranial electrical stimulation (tES), suggests that electrical recordings can be inverted to guide electrical stimulation to specific brain targets (Cancelli et al., 2016; Dmochowski et al., 2017; Fernandez-Corazza et al., 2016; Wagner et al., 2016) and possibly maximize the efficacy of stimulation. The aforementioned features, combined with the perception that tDCS produces only DC artifacts in EEG that are readily filtered, have encouraged trials of concurrent (online) EEG recording during tDCS (Cunillera et al., 2016; Faehling and Plewnia, 2016; Faria et al., 2012; Schestatsky et al., 2013a).

Previous studies that have reported on concurrent tDCS and EEG have employed signal processing of varying complexity to remove what are presumed to be *non-physiological stimulation artifacts* - namely artifacts that arise from non-ideal stimulation and recording amplifier performance (Cunillera et al., 2016; Faehling and Plewnia, 2016; Faria et al., 2012; Mancini et al., 2015; Mangia et al., 2014; Roy et al., 2014). Studies reporting effects of tDCS on the EEG have made varied assumptions about the nature of the stimulation artifact such as: the artifact is narrowband (DC), allowing for simple high-pass filtering; or the artifact is time invariant or spatially stationary, supporting stationary artifact removal techniques (e.g. ICA); the artifact is montage independent, supporting the use of control tDCS montages (i.e. montage/polarity/current specific EEG changes suggest real effects); and/or the artifacts do not outlast stimulation, supporting pre/post (offline) comparisons without need for corrections. These assumptions warrant further testing.

We define *physiological stimulation artifacts* as distinct changes in the voltage on the scalp that reflect physical interaction of applied current with the body - by definition these artifacts are thus inherent (unavoidable) regardless of stimulation or EEG hardware. Of particular concern is the possibility that such physiological artifacts, by failing to meet the assumptions above, may not be removed by conventional signal processing techniques, which can in turn lead to spurious study conclusions. Identifying the mechanisms and features of physiological artifacts supports establishing and applying suitable signal processing techniques and having greater confidence in tDCS outcomes. Indeed, Noury et al. (2016) identified several “non-linear” physiological artifacts plaguing concurrent EEG and tACS likely relating to “rhythmic changes of the body impedance” and referenced analogous issues during tDCS.

Expanding on these observations, we characterize the EEG components during HD-tDCS and identify spatial and spectral profiles of distinct physiological artifacts, as well as their temporal dynamics. We further consider the role of stimulation dose (current, polarity, montage) and device performance (differing current source architectures). Providing a mechanism, we adapt MRI-based computational models of current flow to predict biologic, source-specific changes in scalp voltage (Datta et al., 2013; Huang et al., 2017). We identify inherent physiological artifacts resulting from spatiotemporally-specific impedance changes reflecting: 1) cardiac distortions; and 2) ocular motor distortions. These impedance changes, in turn, produce characteristic dynamic modulations of the

“DC” voltage, which while small relative to the DC offset are nonetheless large in comparison to neurogenic EEG signals. We place these inherent physiological artifacts in the context of non-inherent physiological (myogenic and motion distortion artifacts) and non-physiological (hardware-related) artifacts as well as inherent stimulator artifacts. In this context the non-inherent artifacts are defined as those that are equipment specific (for non-physiological) or related to poor set-up. We consider the degree to which artifacts contaminate and hinder the detection of reliable neurogenic signals in EEG, and the need for refinements to signal processing techniques, specifically towards approaches that recognize features of physiological artifacts.

2. Methods

2.1. Subjects

All experiments were conducted with five neurologically healthy participants (2 females, 3 males) between the ages of 18–40 years (mean: 27.6 ± 8.26 years) at The City College of New York. All procedures were conducted in accordance with the ethical guidelines set forth by the Declaration of Helsinki in 1964 and its later amendments. Experiments were approved by the Institutional Review Board of The City College of New York and written informed consent was obtained from all subjects.

2.2. HD-tDCS

We utilized an HD bipolar (one anode and one cathode) stimulation configuration, where HD electrodes were positioned at standard EEG 10/10 locations. This bipolar HD-tDCS configuration was applied for all stimulation sessions using Ag/AgCl sintered ring electrodes (Soterix Medical Inc., New York, USA), and was prepared using standard HD-tDCS procedures (Villamar et al., 2013). Two bipolar HD montages were investigated: HD-Bifrontal at AF7 and AF8 and HD-MISO at AF8 and C5 (Fig. 1A). The positions of the anode and cathode were interchanged for each montage to accommodate two polarities.

Due to the lack of axiomatic and more accurate terminology in the field of tDCS, the terms anodal and cathodal were adopted for simplicity and convenience in order to distinguish between stimulation electrode polarities. Indeed, in our case, there was no specific cortical target location, so the terminology is arbitrary. Anodal Bifrontal stimulation indicated that the anode was placed at AF7 (over the left supraorbital region or SO) and the cathode was placed at AF8 (over the right supraorbital region); whereas with cathodal Bifrontal stimulation, the anode was placed at AF8 and the cathode was placed at AF7. In the case of anodal MISO stimulation, the anode was placed at C5 (approximately over the left primary motor cortex or M1) and the cathode was placed at AF8 (over the right supraorbital region); whereas for cathodal MISO stimulation, the anode was placed at AF8 and the cathode was placed at C5.

For stimulation, we selected four different types of current source generators, each of which had distinct current output circuit architectures (the manner in which current is maintained over the course of stimulation), and represented common devices used during tDCS. These were used across stimulation sessions, in order to assess current source architecture performance, and to demonstrate artifact reproducibility and device independence. These current source architectures included a digitally controlled voltage-based current source (DCV-CS; 1×1 tES, Soterix Medical Inc.), a digitally controlled resistor-based current source (DCR-CS; 1×1 tDCS, Soterix Medical Inc.), an analog controlled voltage-based current source (ACV-CS; custom built), and a pulse-width modulation controlled current source (PWMC-CS; Activadose II, Caputron Inc.).

Based on prior reports and pilot experiments, the PWMC-CS architecture was selected as a noisy-output, though this current source architecture remains commonly used in tDCS trials. Therefore, for simplicity, results associated with this device architecture is, at times,

referred to as “high-noise.” The DCV and DCR-CS architectures, on the other hand, were selected based on pilot experiments as current source architectures or current sources designed for tDCS with relatively low noise. All results were comparable across the two aforementioned current source architectures, and can be combined and reported as “digital low-noise.” The custom ACV-CS architecture was designed to produce minimal (“floor”) noise and thus served as a lower threshold for noise; results associated with this architecture is, at times, referred to as “analog low-noise”. Across stimulation routines (see *Experimental Design*), the dosages

examined included 0.5, 1.0, 1.5, 2.0 mA, delivered between 0.5 and 10 min. All stimulation device architectures were utilized during stimulation routine 2, whereas only the ACV and DCV-CS architectures were used for stimulation routine 1 and 3, respectively.

2.3. Experimental design

In order to systematically elicit and examine artifact characteristics, we utilized three main stimulation routines, all consisting of concurrent

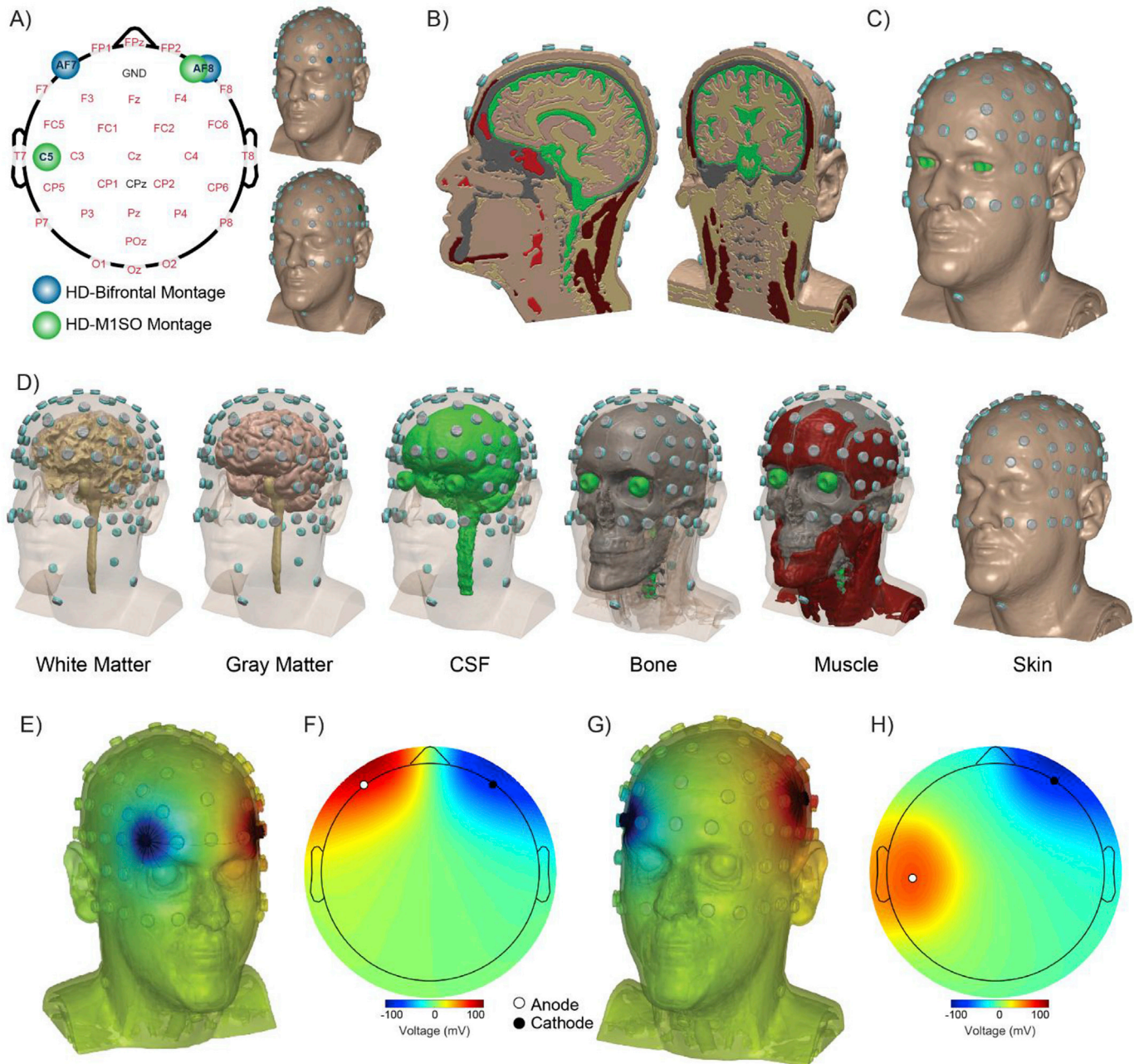


Fig. 1. Stimulation and EEG montages, and model architecture. A) EEG cap layout and integrated stimulation sites for HD-Bifrontal and HD-M1SO stimulation. MRI-derived head models including scalp locations of stimulating electrodes for HD-Bifrontal stimulation (top, blue electrodes), HD-M1SO stimulation (bottom, green electrodes), and select EEG recording electrodes (gray). B) Sagittal and coronal views of an exemplary subject’s head model indicating tissue volume layers of the computational model used. Cardiac artifacts were modeled by applying a skin conductivity change. C) Ocular motor distortions, specifically blinks, were modeled by adjusting the conductivity of the eyelids. D) Computational models used included layers of white matter, gray matter, CSF, bone, muscle, fat (not shown), and skin. E) Skin DC voltage distribution predicted by the computational models for 2 mA of anodal HD-Bifrontal stimulation. F) Topographic voltage distribution for 2 mA of anodal HD-Bifrontal stimulation from model predictions. G) Skin voltage distribution predicted by the computational models for anodal HD-M1SO stimulation. H) Topographic voltage distribution for anodal HD-M1SO stimulation from model predictions. Note that all model scalp topographies were sampled at EEG recording sites for stimulation, colorbars indicate voltages for both computational models’ skin voltage and scalp topographic distributions.

(online) EEG and tDCS, meaning EEG data were acquired during the delivery of current with tDCS. In all experiments (routines) EEG was first acquired with the stimulator connected to the HD electrodes on the headgear but not powered (baseline not powered) and with the stimulator then powered on but no tDCS applied (baseline or 0 mA). All analysis of artifacts was made in relation to baseline (power on, 0 mA) conditions unless indicated otherwise. With the exception of eliciting myogenic artifacts by jaw clenching and performing head rotations, during all stages of data acquisition subjects were asked to sit comfortably and fixate on an arbitrary point of their choosing, directly ahead of them. Respecting IRB protocol limitations on cumulative dose per experimental session, each routine was designed to assess a different artifact characteristic - with the main difference between routines being the length of the stimulation block. Routine 1 consisted of short stimulation periods, allowing for the testing of more current increments; routine 2 consisted of intermediate stimulation length, allowing for the application of multiple current sources with a fixed current intensity; and routine 3 consisted of the longest stimulation length with a fixed current source and intensity. None of the results are qualitatively routine specific.

Stimulation routine 1 consisted of a Bifrontal montage (at standard locations AF7 and AF8; see Fig. 1A) with HD-tDCS. This was conducted using the ACV-CS architecture, and applying repeated, randomized stimulation intensities. In this stimulation routine, current intensities of 0.5, 1.0, 1.5, and 2.0 mA were randomized and each was applied three times for 30 s, with 1 min off intervals (device powered on), during concurrent EEG, in one recording block. Polarity (anode/cathode) was altered across two stimulation blocks.

Stimulation routine 2 consisted of an anodal M1SO montage (at standard locations AF8 and C5; see Fig. 1A), 2.0 mA current intensity for 1 min, repeated with all four different current source architectures (DCV-CS, DCR-CS, ACV-CS, PWMC-CS), and was administered in a randomized order. Baseline (device powered off) EEG was recorded before applying any stimulation, and prior to the commencement of each stimulation session (pre; device powered on but not stimulating). EEG recording blocks consisted of a pre stimulation period (prior to the commencement of stimulation, device on but not stimulating), during stimulation (concurrently recording EEG during the administration of tDCS), then up to 3 min post stimulation (after the cessation of stimulation). This procedure was repeated with all four different current source architectures with at least 15 min between blocks.

Stimulation routine 3 consisted of an extended stimulation time, over alternating stimulation polarities (anodal/cathodal), while utilizing the DCV-CS architecture (a digital low-noise device). With this stimulation routine, 1.0 mA of current was applied for 10 min with a two-polarity (anodal/cathodal) M1SO montage. This procedure consisted of 5 min EEG prior to stimulation (pre; device powered on) as well as 5 min after stimulation (post; device powered on). For all stimulation routines at least 1 min of resting state EEG was collected before any intervention (baseline, device powered off).

In order to elicit non-inherent physiological artifacts, subjects were instructed to perform exaggerated movements, contrary to what is expected in standard EEG data acquisition. In the case of non-inherent physiological myogenic or muscle artifacts, subjects were asked to contract then relax their jaw muscles for up to 2 s at a time (while keeping teeth aligned and together). This was repeated at least 5 times under 0, 1, and 2 mA of anodal Bifrontal stimulation. Motion distortion artifacts were elicited by instructing subjects to perform slow, rotational head movements followed by swift left and right head tilts for up to 2 min, under 2 mA of cathodal M1SO stimulation.

In order to demonstrate artifacts associated with switching on a current source during concurrent EEG acquisition (“device on” artifact), we acquired data prior to, and after switching on (but not applying stimulation) a connected current source (DCV-CS). Stimulation electrodes were placed at cathodal M1SO locations (cathode: C5 and anode: AF8). To demonstrate device saturation, HD-tDCS was applied with the ACV-CS, at electrodes at AF7 (anode) and PO8 (cathode). The stimulation

intensity was manually increased and incremented from 0.5 to 4 mA in steps of 0.5 mA while holding the current intensity constant for 25 s at each increment.

2.4. EEG recording and analysis

Data were acquired using a 32-channel waveguard cap (ANT Neuro, The Netherlands) with 29 integrated HD holders (Soterix Medical Inc.). Electrode positions were based on the 10/10 international system. EEG signals were amplified using an eego sport amplifier (ANT Neuro, The Netherlands), sampled at 2 kHz, and recorded relative to a CPz reference. The amplifier had a bandwidth of 0–520 Hz, the signal range was set to 1 V peak-to-peak, and data were online grounded to AFz. Prior to the commencement of each EEG recording, scalp impedances were verified to be below 20 k Ω .

All offline analysis was performed using in-house scripts written in MATLAB (R2015b; MathWorks, Natick, MA) with raw data-reading, and topographic plot functions from the EEGLAB toolbox (Delorme and Makeig, 2004). Recordings (with and without stimulation) were baseline corrected by subtracting the mean voltage amplitude from each electrode, across all 32 EEG electrodes, between 1 and 25 s after the commencement of the EEG recordings (unless stated otherwise). During trials where HD-tDCS was applied, at least 30 s elapsed before stimulation ramp-up began and 30 s after stimulation ramp-down ended. For time series analysis, a least-squares linear fit subtraction was applied, when necessary, over the stimulation periods in order to reduce the DC voltage offsets and inherent drifts. For visualization and quantification of low frequency processes over time, data were low-pass filtered below 5 Hz or bandpass filtered between 0.5 and 5 Hz, when necessary, with a 2nd order Butterworth filter. Power spectrum and power spectral density (PSDs) calculations were performed using the Welch's power spectral density estimate and the short-time Fourier transform, respectively, with a 5 s Hamming window and 4.75 s overlap (unless stated otherwise).

2.5. Physiological monitoring

During concurrent HD-tDCS and EEG recordings, subjects' cardiac activity, respiration, ocular motor activity, and head motion were monitored. Both cardiac activity and ocular motor activity, were monitored using bipolar snap-on electrodes. For cardiac activity, bipolar electrodes were placed across subjects' chest approximately 5 cm below the medial clavicle, whereas for ocular motor activity, electrodes were placed below the subjects' right eye and at the outer canthus of the eye. This was used as a reference for blink timing, while EOG data were extracted from electrodes FP1 and FP2. Respiration was monitored using a breathing belt placed off-center across subject's chest, below their pectoral muscles. Head motion was monitored with an accelerometer secured at the top of subject's head at standard point CPz. All physiological monitoring data were time-locked to EEG data.

2.6. Computational models

A T1-weighted MRI scan was acquired for an exemplary subject. This was then converted into a subject-specific, high resolution, finite element method (FEM) model. The FEM model was then used to predict voltage distributions on skin during stimulation. These subject-specific voltage distributions were subsequently compared to EEG voltage distributions acquired during stimulation. The coefficient of determination (R^2) was computed between each model and corresponding physiological artifact, in order to assess the computational models' performance.

Automated segmentation was performed in order to segment MR images into six different tissues (Fig. 1D) using algorithms within Statistical Parametric Mapping (SPM8, Wellcome Trust Center for Neuroimaging, London, UK). In-house MATLAB scripts were used to smooth scan artifacts, remove model discontinuities, and implement 10/10 EEG electrodes/gel using common anatomical landmarks (Huang et al.,

2013): nasion (Nz),inion (Iz), pre-auricular right (PAR) and pre-auricular left (PAL). We added fat and several cephalic tissue groups including the epicranial aponeurosis, occipitalis, masseter, frontalis and temporalis through manual segmentation and imaging techniques of ScanIP (Simpleware Ltd, Exeter, UK). The following electrical conductivities were assigned to each tissue layer and scalp electrode (in S/m): skin = 0.456, fat = 0.025, muscle = 0.4, skull = 0.01, CSF = 1.65, gray matter = 0.276, white matter = 0.126, air = 1×10^{-15} , electrode = 5.8×10^7 and gel = 1.4 (Bikson et al., 2012; Datta et al., 2009). Model scalp voltages were referenced to standard location CPz and were generated for each stimulation montage.

Based on experimental observations, we simulated three types of physiological artifacts: cardiac, ocular motor, and myogenic. In each case, we tested a hypothesis about the origin of the physiology-specific artifacts on the changes in the spatial profile of scalp potentials produced during tDCS. With each case, the quasi-static solution was determined by evaluating the difference between baseline stimulation states and case specific simulated activity, which produced a simulation of the peak changes in scalp voltage. In each case, parameters were as follows:

- 1) Cardiac distortion: We modeled a 0.3% increase in global scalp conductivity corresponding to systolic dilation of blood vessels in skin (Fig. 1B). Based on our hypothesis, this represented the impedance changes associated with the cardiac distortion (Eyuboglu et al., 1989; Ngai and Jones, 2013).
- 2) Ocular motor distortion: We modeled blink responses by segmenting skin over the eye (Fig. 1C) and computing the resultant voltage distribution between conditions with skin over the eye and without. Due to overestimation of eyelid volume in the generated model, which was dictated by the MRI resolution (1 mm³ voxel), the conductivity of eyelids was increased by factor of 2.8 (~3 times skin conductivity). Based on our hypothesis, this represented an impedance change associated eyelid closure or blink distortions (Iwasaki et al., 2005).
- 3) Myogenic distortion: We modeled the consequences of jaw clenching as an isometric muscle contraction leading to an increase in muscle resistivity (Li et al., 2016; Shiffman et al., 2003). In this case, the craniofacial muscle groups that were involved in baseline EMG activity were segmented and “active” tissue properties (lower conductivity: 10^{-4} S/m) were assigned to this selected group in order to generate scalp voltages in an active state, while baseline stimulation conditions were represented as normal muscle properties (Fig. 8F). Based on our hypothesis, this represented an isolated impedance change associated with myogenic activity.

3. Results

3.1. General characteristics of DC voltage

During HD-tDCS, the application of an external direct current increased the recorded voltages on all 32 EEG electrodes. Across protocols (routines, montages, currents) tested, the largest deviations in voltage tracked the applied current: increasing to a value during the tDCS ramp-up, generally maintaining the value (the “DC offset”) during the sustained current phase, and decreasing along with the tDCS ramp-down. The largest positive and negative voltage deviations, across protocols, were observed near the anode and cathode, respectively. These polarity specific offsets indicated that the DC offset was montage specific. In all observed cases, applying 2 mA of current during tDCS produced a DC offset that was up to 1000 fold larger than baseline neural EEG signals (Fig. 2A). The two digital low-noise devices (DCV-CS, DCR-CS architectures) and analog low-noise device (ACV-CS architecture) produced offsets that were, by inspection, dominated by low frequency (“DC”). The high-noise device (PWMC-CS architecture), however, produced a signal with significant broadband fluctuations (Fig. 2E; cf. Roy et al., 2014; Salimpour et al., 2016). The spatial distribution of this broadband noise approximated the DC-shift (Fig. 2B During Stim), which uncorrected

would appear to be a montage specific “signal”.

The topographic voltage distribution of the DC voltage, predicted by computational models matched those acquired in EEG for 2 mA of anodal HD-Bifrontal and cathodal HD-MISO stimulation (Fig. 1F and H). The model-derived skin DC voltage predicted the distribution of stimulation voltages across the scalp and head, where the largest voltages were directly under the stimulation electrodes (Fig. 1E and G).

Across protocols, the DC offset changed incrementally (“drift”) while stimulation was sustained (Hahn et al., 2013), this fractional change (up to ~3 mV or 2% of the DC offset over 50 s with 2 mA of current) was still larger than neurogenic EEG signals. Across protocols, there was a residual DC offset present post stimulation, and was evident for up to approximately 1 min after the end of the ramp-down (Fig. 2C). This post stimulation offset was significantly less than the peak DC offset during stimulation but on the order of magnitude of drift in the DC offset during stimulation (~1.5 mV). Across current source architectures, the spatial distribution of the scalp voltages of the residual DC offset was comparable to that of the DC offset during stimulation, having the largest positive and negative values near the anode and cathode electrodes, respectively (see Fig. 2B Post Stim).

3.2. General spectral profile

Power spectral densities (PSDs) were calculated over the pre, during, and post stimulation periods using an exemplary EEG electrode FC5, which was closest to the stimulation cathode (C5, Fig. 2D). Broadband harmonic distortions were evident during the ramp-up/ramp-down periods of the stimulators as a result of the stepwise escalation/de-escalation of current and resultant stepwise voltage amplitude. These broadband distortions contaminate neurogenic EEG signal during the ramp periods. During stimulation, significant power at low-frequencies (~0 Hz) reflected the DC offset. Stimulation introduced power in the EEG, increasingly below 10 Hz at recording sites near stimulation electrodes, with a local peak at ~1 Hz (Fig. 2E). This was consistent with a physiological source and was comparable across stimulation device architectures, with the exception of the noisy device, which had high-power broadband distortions across all physiologically-related frequency bands.

3.3. Linearity of DC voltage

We quantified the relationship between the applied currents and scalp voltages, with two polarities (anodal/cathodal) using stimulation routine 1. Voltage amplitude offsets during stimulation were corrected relative to the preceding off period. Voltage at each electrode increased linearly with current intensity (Fig. 3) such that the relative spatial distribution was maintained (Fig. 3 topoplots). The mean voltage amplitude across applied current intensities for both anodal and cathodal stimulation was linearly correlated across EEG electrodes (Fig. 3) and for each recording electrode, spatial changes in voltages (mV/mA) between current intensities was comparable, across the scalp (Fig. 3 topoplots), providing value for artifact removal, especially in cases of similarly distributed physiological artifacts (see Discussion).

3.4. Cardiac artifact

Across protocols, artifactual modulations were present in raw EEG data during all stimulation periods. Of these modulations, low frequency, heartbeat-locked oscillatory activity was predominant and was characterized as a full cycle, periodic, complex wave that rose/fell in voltage, relative to the heart beat. Analogous to the DC offsets, this activity was maximal in electrodes closest to the stimulating electrodes in a montage specific manner.

With stimulation routine 2, EEG electrodes FC6 and CP5 were selected to highlight the cardiac related oscillations or cardiac artifacts since they were in close proximity to the anode and cathode and had

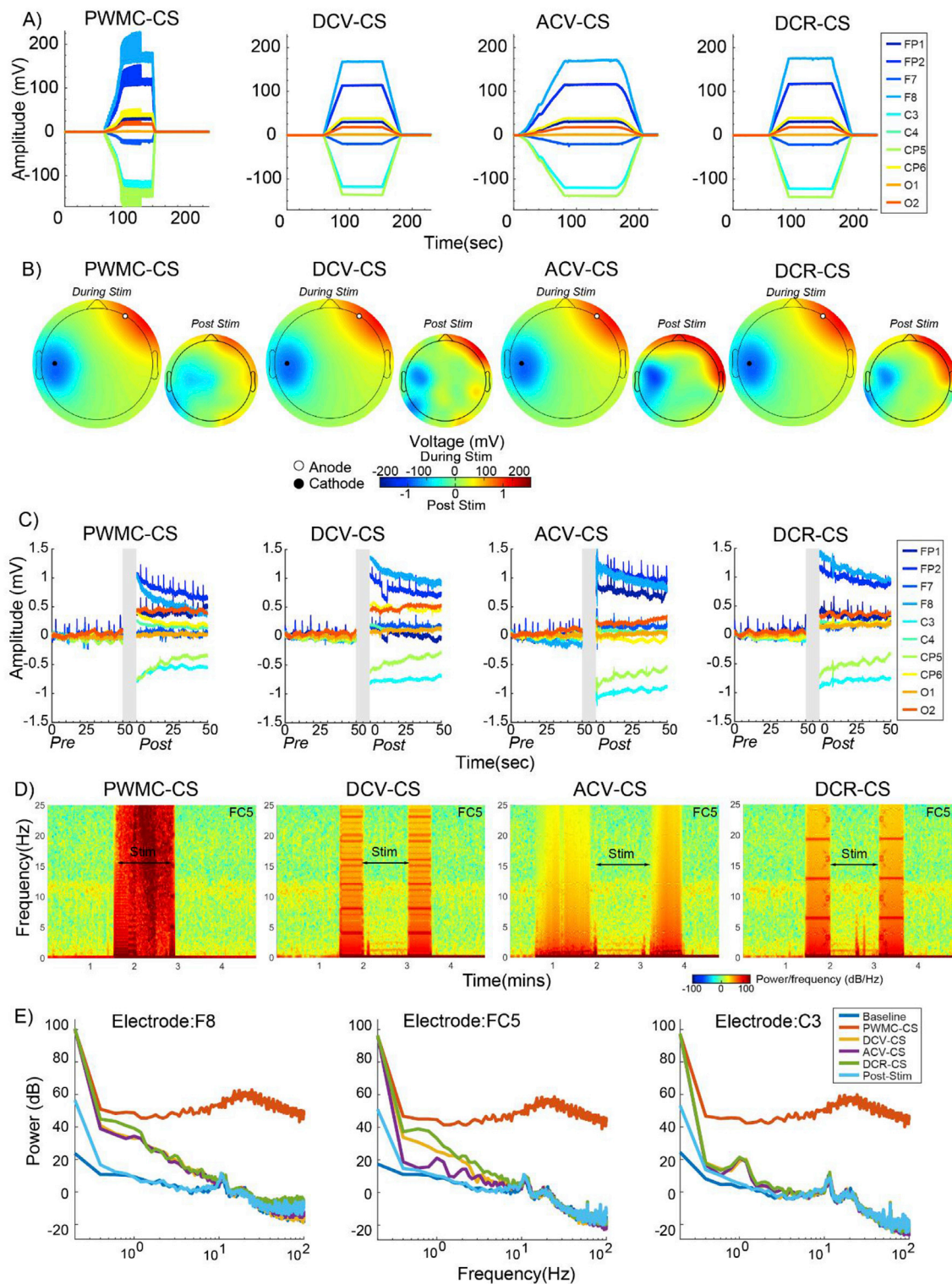


Fig. 2. DC offset and spectral content of EEG during and after MISO tDCS, across current source architectures. A) Voltage over time using different current source architectures. Linear ramp-up and ramp-down periods were present at the beginning and end of the stimulation period. B) Mean scalp topographies, over each stimulation period, were comparable in magnitude and distribution across current source architectures and the largest voltage amplitudes were present near the anode (AF8) and cathode (C5). Mean voltage topographies, post stimulation, revealed the presence of residual scalp voltage across current source architectures. C) Post stimulation, when current was no longer being delivered, electrodes decayed in voltage over a 50 s period. D) Spectrograms (from FC5) showed broadband distortions produced during the ramp-up and ramp-down periods. Low-frequency spectral density offsets, produced during stimulation and post stimulation, were present. Note that the time period shown is identical to panel A. E) Across current source architectures, EEG electrodes had large power offsets at low frequencies (0–10 Hz) and pronounced peaks (1–1.2 Hz) during stimulation (except the PWM-C-S), compared to baseline and post stimulation. Note that the spectra during stimulation were computed over the same stimulation time period in panel A and D (excluding ramp-up and ramp-down).

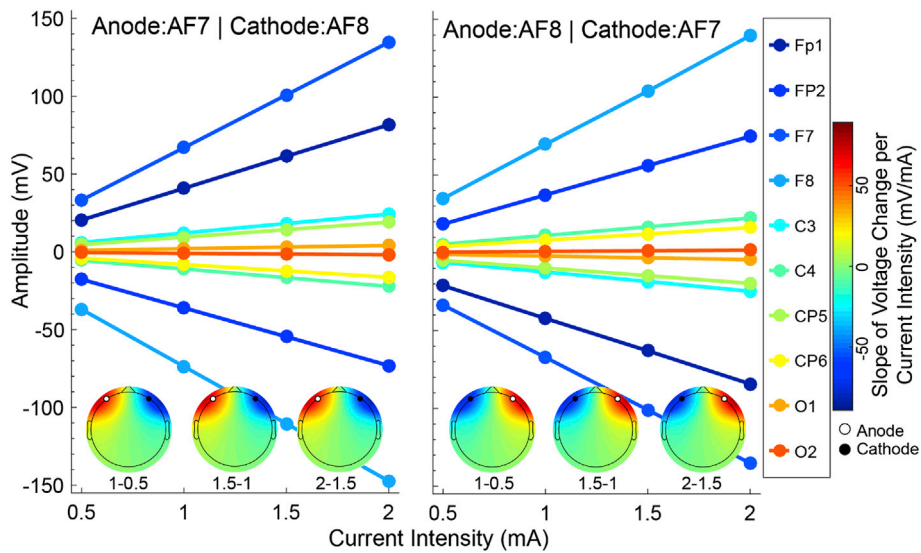


Fig. 3. Linearity of DC artifact in EEG during Bifrontal tDCS. The mean voltage amplitude across applied current intensities for both anodal (left) and cathodal (right) stimulation was linearly correlated across the majority of EEG electrodes. The change in voltage between current intensities (mV/mA) had identical spatial patterning across the scalp for different current intensities.

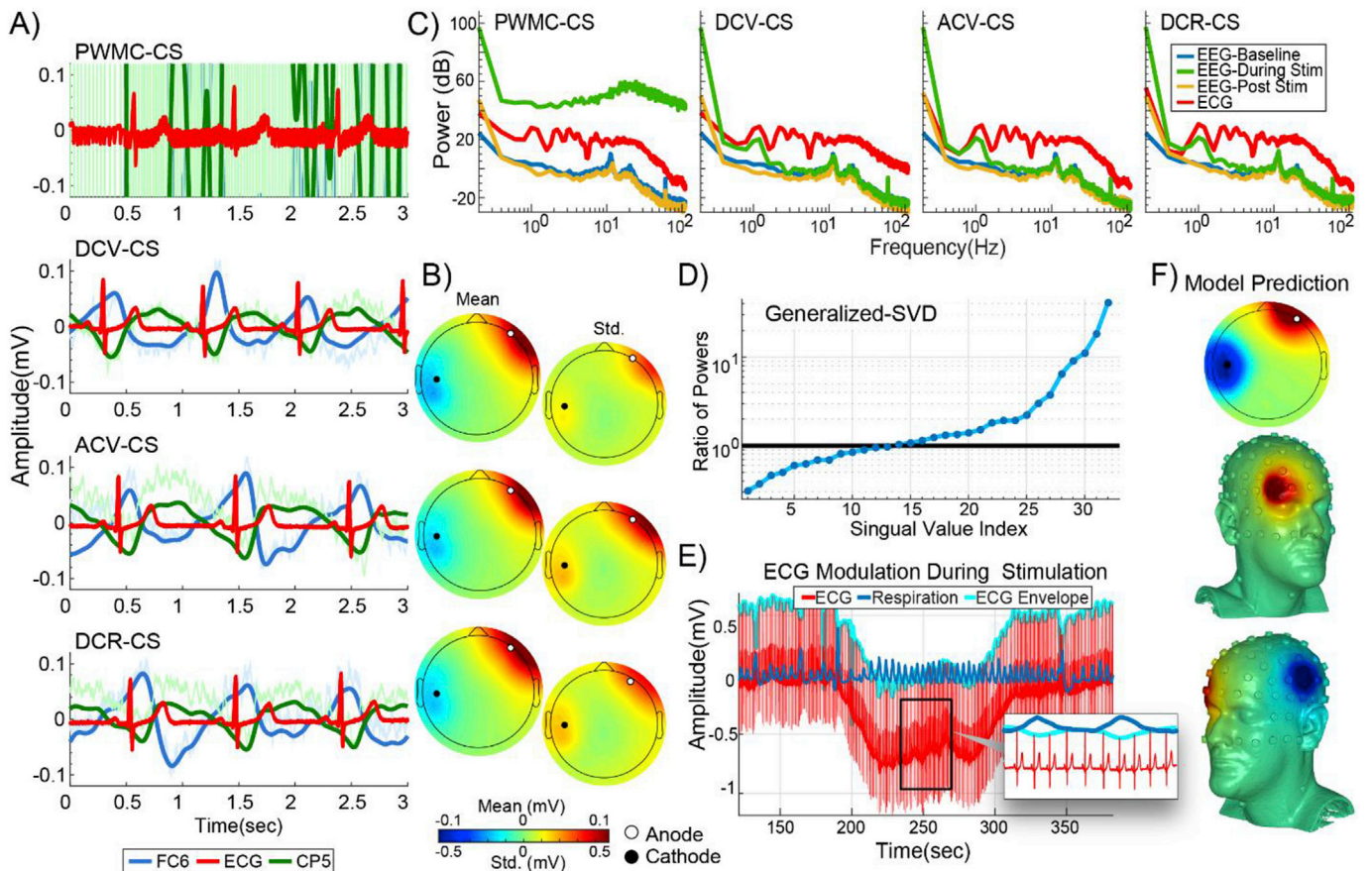


Fig. 4. Experimental and simulated EEG cardiac artifact during MISO tDCS, and ECG; current source independence. A) The cardiac artifact in EEG data was evident and consistent across current source architectures (except the PPMC-CS). Unfiltered, detrended traces for FC6 (light blue) and CP5 (light green) are shown for comparison. ECG signals are scaled down for comparison. B) Mean and standard deviation (Std.) scalp topographies during the peak of the cardiac artifact across the DCV, ACV, and DCR-CS architectures. Colorbar for the mean (mV) applies to panel B and F. C) Comparison of ECG; and EEG baseline (not powered), during, and post stimulation at electrode C3. D) The generalized singular value spectrum resulting from analysis of the EEG with and without tDCS. E) ECG, ECG envelope and respiration signals (arbitrary units) over time with linear changes in the ECG voltage during the stimulation ramp-up and ramp-down periods. During stimulation, the overall ECG signal had a pronounced DC offset and the ECG envelope remained phased shifted with respiration. F) Computational model prediction of the spatial scalp voltage distribution of the cardiac artifact during 2 mA of cathodal MISO stimulation in 2D and 3D.

minimal blink interference. Data during stimulation were detrended (to remove the DC offset; Fig. 4A light colors) then bandpass filtered between 0.5 and 5 Hz (Fig. 4A dark colors) to highlight the low frequency cardiac artifact. The artifact was reproducible across all current source architectures with the exception of the PWMC-CS architecture; which produced large-amplitude high-frequency, broadband noise in EEG data (Fig. 2D PWMC-CS) as well as in ECG electrodes (Fig. 4A). When paired with concurrent ECG the oscillatory cardiac artifact on the scalp had a consistent phase delay following the QRS complex and preceding the T-wave of the ECG signal (Fig. 4A). This temporal precision indicates the artifact was cardiac-related, and also independent of current source architectures (stimulation device independent). The artifact showed polarity dependence, where electrode FC6 (near the anode) had a positive deflection and electrode CP5 (near the cathode) had a negative deflection, both of which were time-locked with each other and peaked after the QRS complex in the ECG (Fig. 4A). Mean and standard deviation of scalp topographies of the peaks of the cardiac artifact reflected the DC artifacts produced by the stimulation montage (Fig. 4B). With the spatial scalp distribution of the cardiac artifact, a maximal negative voltage was present nearest the cathode and maximal positive voltage was present nearest the anode; as proximity increased from the stimulation electrodes the artifact was attenuated (Fig. 4. B).

In the frequency domain, a comparison of ECG and EEG baseline (not powered), during, and post stimulation revealed a prominent peak at 1–1.2 Hz for both the ECG and EEG during stimulation conditions, but not for EEG baseline (not powered) and post stimulation (Fig. 4C). The

ECG-locked frequency peak was evident across different current source architectures (with the exception of the PWMC-CS), which corroborated the artifact's current source architecture independence (stimulation device independence) and consistent with a physiologic origin. A ratio of the generalized singular values (similar to a signal to noise ratio) between stimulation and non-stimulation conditions, which was computed using the Generalized Singular Value Decomposition (GSVD), showed that the EEG during stimulation contained 5 spatial components (Index 28–32) whose power was 5 times higher than that observed without stimulation. This suggests that the stimulation artifact is high-dimensional, and that its removal would likely distort the genuine EEG (Fig. 4D).

During stimulation, the ECG signal, like cephalic EEG signals, had a DC offset (up to a range of 0.5–1 mV; Fig. 4E). Linear changes in voltage during the stimulation ramp-up and ramp-down periods were also present in the ECG signals, however the inverse relationship between respiration and the envelope of the ECG remained unaffected during stimulation (Fig. 4E). The DC offset in ECG electrodes was present across all stimulating devices and indicated that the applied current produced extracephalic skin voltage changes which were detectable at least as far as the upper torso.

By simulating skin conductivity changes in computational head models (see methods), the cardiac artifact was emulated. By taking the difference in the model's resultant scalp voltages between altered and unaltered skin conductivity, models reproduced both the magnitude and the spatial distribution of the cardiac artifact. Like the cardiac artifact detected in acquired EEG data for cathodal MISO stimulation, the model

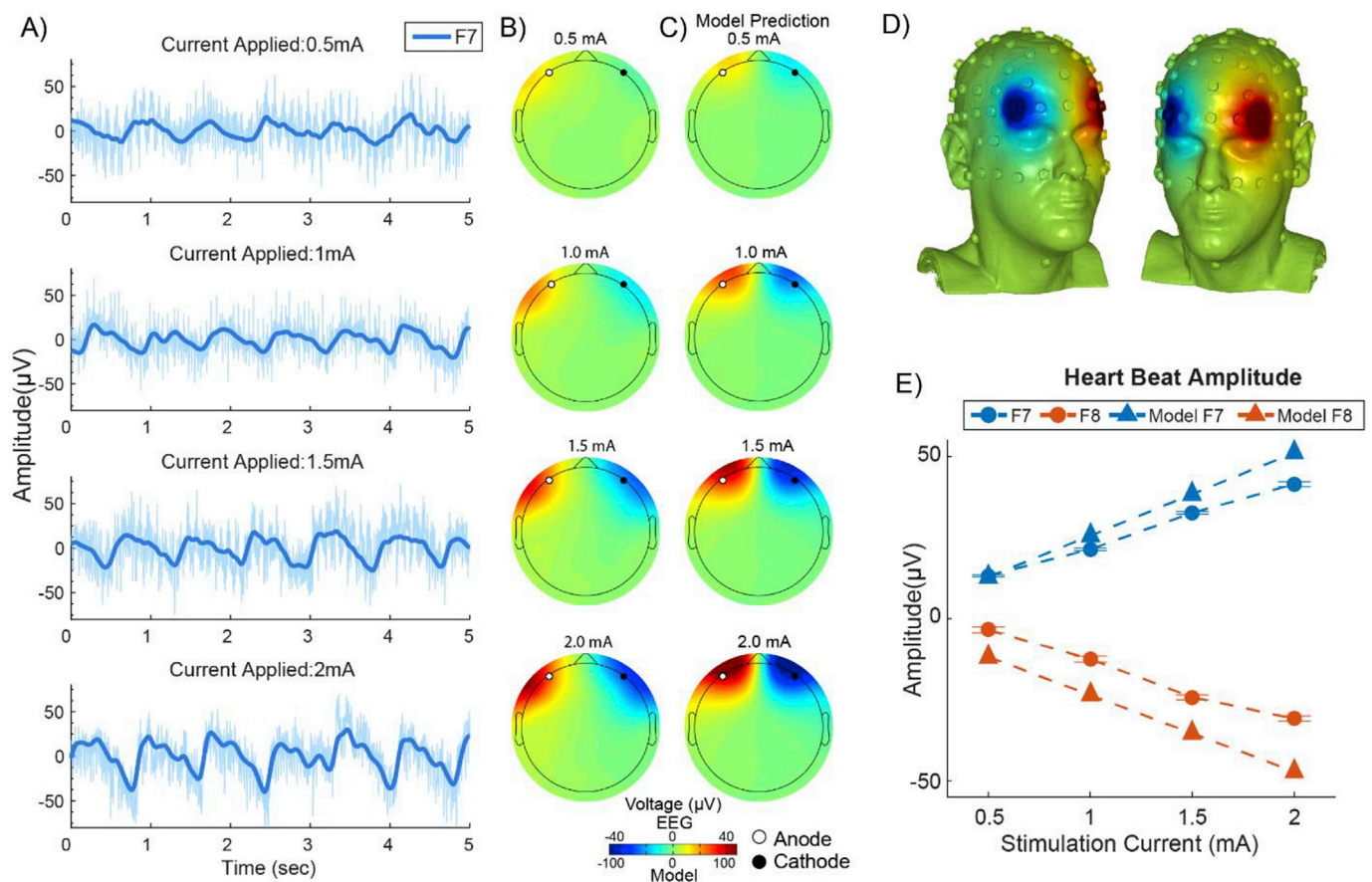


Fig. 5. Experimental and simulation cardiac EEG artifact during Bifrontal tDCS, and role of stimulation intensity. A) The cardiac artifact over time with applied current intensities of 0.5, 1.0, 1.5, and 2.0 mA. Detrended raw traces (light blue) are shown together with detrended and filtered traces (dark blue). B) Mean scalp topographies at the peak of the cardiac artifact during 0.5, 1.0, 1.5, and 2.0 mA of applied current. C) Spatial distribution of the cardiac artifacts' voltage propagation predicted by computational models at 0.5, 1.0, 1.5, and 2.0 mA of applied current. Model colorbar applies to panel C and D. D) Computational model prediction of the spatial scalp distribution of the cardiac artifact during 2 mA of Bifrontal stimulation in 3D. E) Mean and SEM of cardiac artifacts' peaks, detected at F7 and F8, during stimulation and derived from the computational models for current intensities of 0.5, 1.0, 1.5, and 2.0 mA.

predicted extrema over the right supraorbital and motor cortex locations (Fig. 4F). Model derived scalp voltage (Fig. 4F) and the cardiac artifacts' scalp voltage, during 2 mA of cathodal MISO stimulation (Fig. 4B), across devices, were correlated and the computational model accounted for 63%, 59%, and 69% of the variance (as indicated by R^2) for the DCV, ACV, and DCR-CS respectively. This prediction was consistent with the hypothesis that tDCS first creates a montage specific distribution of scalp voltage that is then modulated at each pulse by a global change in scalp impedance.

During stimulation routine 1, the dynamics of the cardiac artifact with varying degrees of current intensities was identified (Fig. 5A). To highlight the artifact, data were detrended (Fig. 5A light blue) and bandpass filtered between 0.5 and 5 Hz (Fig. 5A dark blue). With anodal Bifrontal stimulation (anode: AF7, cathode: AF8), the cardiac artifact's voltage offsets were maximal at the frontal electrodes. The artifact was observed throughout all trials of each current intensity delivered, increased in amplitude over 0.5–2 mA of applied current (Fig. 5A) and had a spatial distribution consistent with the stimulation montage (Fig. 5B). At electrode F7 and F8, subject-specific cardiac artifacts increased in amplitude with increasing current intensity (Fig. 5E).

Again, assuming skin impedance changes, a computational model simulated the cardiac artifact's spatial distribution and magnitude of Bifrontal stimulation. The model predicted anterior recording electrodes would undergo higher voltage amplitude changes during a pulse, with decreasing voltage deviation with increasingly posterior electrode location (Fig. 5D). Similar to the artifacts scalp voltage distribution, the

model prediction of the spatial distribution of the cardiac artifact changed linearly with increased current intensity (see Fig. 5C). Model derived scalp voltage (Fig. 5C) and the cardiac artifacts' scalp voltage (Fig. 5. B), across current intensities, for anodal Bifrontal stimulation were correlated and the computational model accounted for 46%, 55%, 56%, and 55% of the variance (as indicated by R^2) for 0.5, 1.0, 1.5, and 2.0 mA of stimulation, respectively. As observed experimentally, the model predicted both an increase in magnitude and area of the artifact with increasing current intensity. Experimental cardiac artifact's peak voltage offset at specific electrodes (F7 and F8) were approximated by the computational models (Fig. 5E).

3.5. Ocular motor artifact

During stimulation, significant modulatory effects in amplitude and polarity were observed in relation to ocular motor or blink responses. Amplitudes of these physiological responses were highly variable across stimulation current intensities as well as across stimulation montages. The spatial distribution of scalp voltages during blink responses were observed to be altered during stimulation, in a stimulation montage specific manner.

With the application of stimulation routine 2, during the pre and post stimulation time periods, both FP1 and FP2 detected positive blink deflections. During the course of 2 mA cathodal MISO stimulation (anode: AF8, cathode: C5) the blink responses at FP2 (near the anode) reversed in polarity to a high amplitude negative deflection, whereas blink responses

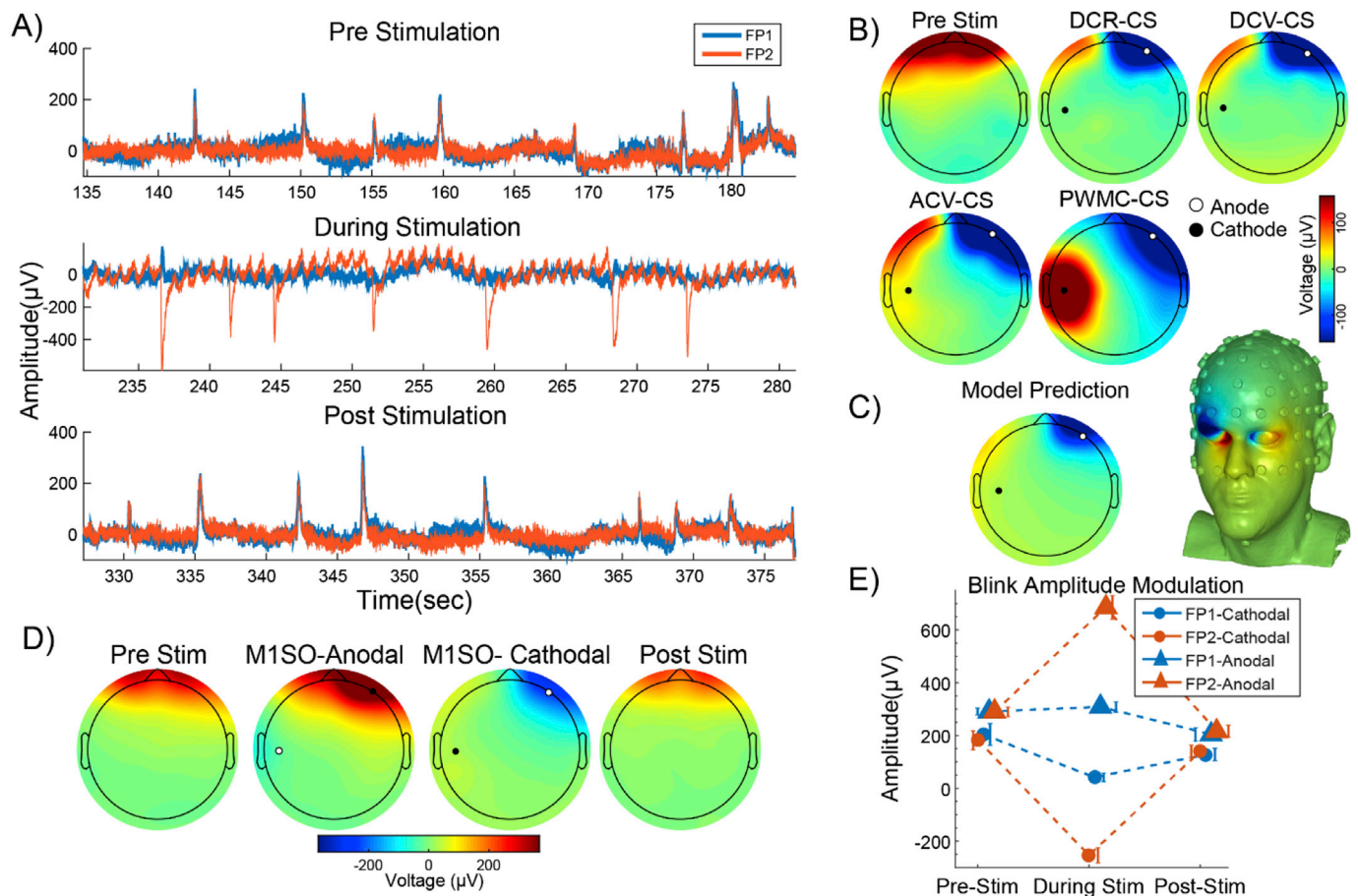


Fig. 6. Experiment and simulation of ocular artifact in EEG during MISO tDCS. A) Pre and post-stimulation, EOG at both FP1 and FP2 showed positive blink deflections. During 2 mA of MISO stimulation blink deflections decreased in amplitude and reversed in polarity for FP1 and FP2, respectively across current source architectures. B) The mean spatial distribution of blink responses taken at the peak of blink deflections pre and during 2 mA of MISO stimulation, across current source architectures. Note that the colorbar applies to panel B and C. C) Computational models were able to predict both the magnitude and the spatial distribution of the blink responses on the scalp. D) Distribution of blink scalp topographies differed between cathodal and anodal MISO stimulation (1 mA). E) Blink amplitude change for FP1 and FP2 over pre, during, and post stimulation with 1 mA of anodal and cathodal stimulation.

at FP1 decreased in amplitude but remained positive (Fig. 6A During Stimulation). This asymmetric modulation of the blink response by cathodal M1SO tDCS was reproduced across stimulation current source architectures (with the exception of the PWMC-CS). Over the stimulation period, alterations to blink responses remained stable and cardiac artifacts were observed interleaved between blink deflections, highlighting both artifacts' overlap and concurrence during stimulation (see Fig. 6A During Stimulation). Blink responses were isolated by utilizing a peak detection algorithm to identify exemplary voltages, the scalp voltage distribution at these time points were isolated and averaged across blink responses resulting in the spatial distribution of the blink responses. Compared to pre-stimulation conditions, where bifrontal positive dipoles were present over both eyes, during stimulation, a negative monopole was present in electrodes over the right SO locations (near the anode) and a positive monopole was present in electrodes over the left SO locations. This distribution was observed across current source architectures with the exception of the PWMC-CS (Fig. 6B).

In contrast to the effects of cathodal M1SO tDCS, anodal M1SO tDCS (1 mA) increased the positive amplitude of the blink response in FP2 (the electrode near the cathode; Fig. 6D, E). Consistently across montages and polarity (anode/cathode) near an orbit there were decreases/increases in blink amplitude, in a device independent manner.

A computational model was used to investigate the etiology of the altered blink responses during concurrent EEG and tDCS. In order to model change in scalp potential by blinking during tDCS, the conductive properties of the eyelids were altered to simulate eyes open and closed conditions (Fig. 1C). The difference in predicted scalp

potentials between eyes open and closed conditions, approximated the topography of the experimental blink offset during tDCS (see below). Model derived scalp voltage (Fig. 6C) and the blink responses' scalp voltage (Fig. 6B), during 2 mA of cathodal M1SO stimulation, across devices, were correlated and the computational model accounted for 47%, 86%, 82%, and 84% of the variance (as indicated by R^2) for the PWMC, DCV, ACV, and DCR-CS respectively. The computational model also accounted for 87% and 78% of the variance for the blink responses, during 1 mA of anodal and cathodal M1SO stimulation (Fig. 6D), respectively.

Under stimulation routine 1, the effect of incrementally increasing current intensities on blink responses was observed. Using anodal Bifrontal stimulation (anode: AF7, cathode: AF8), blink responses at frontal electrodes diverged in peak amplitude with increased current intensity. At 0 mA of applied current or no stimulation, blink responses were both locked in amplitude and latency (Fig. 7A). When the current increased from 1 to 2 mA, at FP1 (near the anode) blink responses decreased in amplitude whereas responses at FP2 (near the cathode) increased in amplitude (Fig. 7A). The cardiac artifact was also seen interleaved between blink deflections and were most obvious at 2 mA of applied current. With no stimulation, the spatial voltage distribution of the blink response had positive supraorbital dipoles, which shifted to a right supraorbital monopole with the application of 1 and 2 mA of current (Fig. 7B). For anodal Bifrontal stimulation, subject-specific average blink response amplitudes over the course of stimulation compared to pre stimulation at FP1 decreased whereas at FP2 blink responses increased (Fig. 7C). Normalizing blink spatial topographies during stimulation to

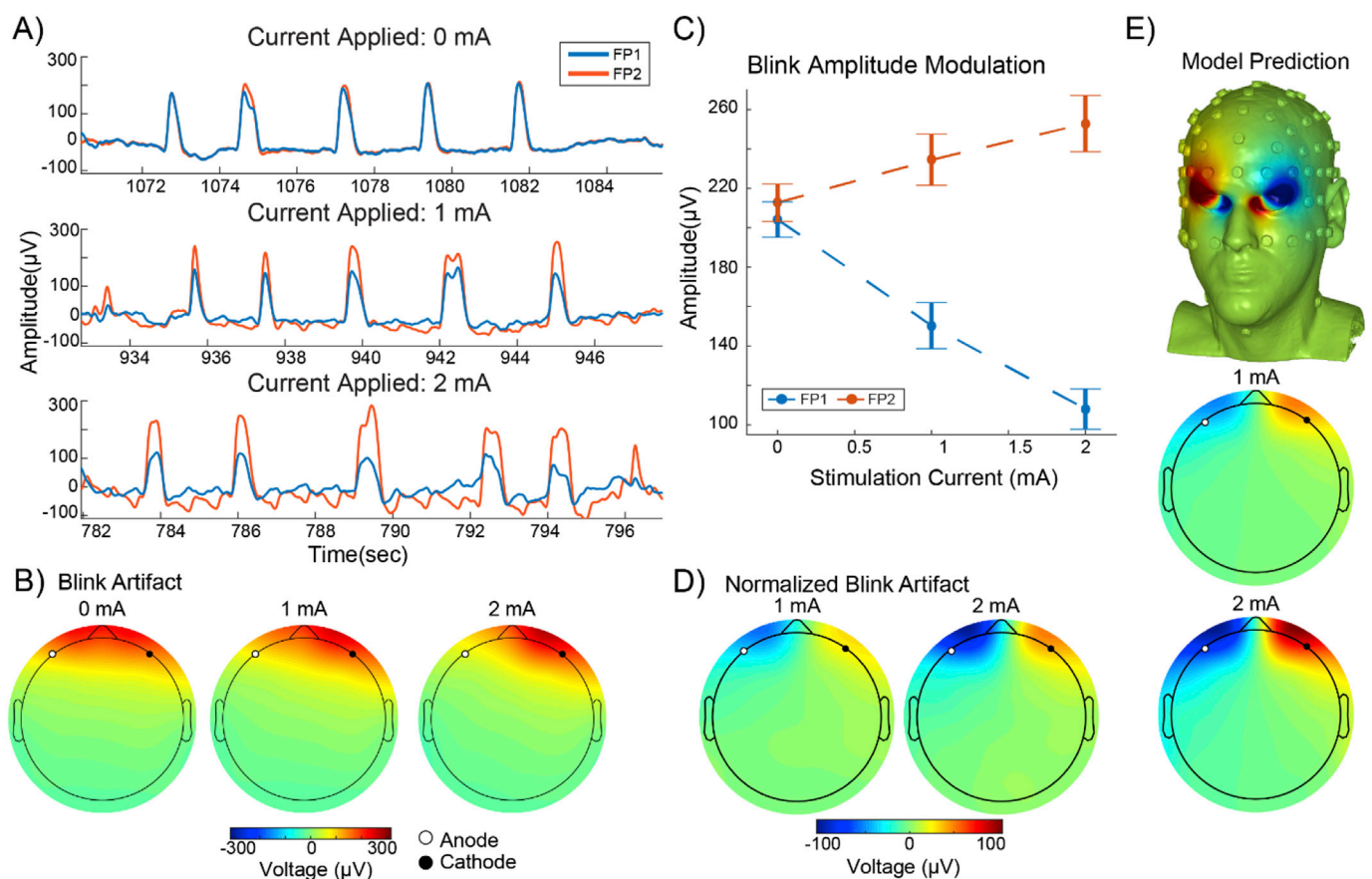


Fig. 7. Experiment and simulation of ocular artifact in EEG during Bifrontal tDCS, and role of current intensity. A) Blink deflections at FP1 and FP2 over time during 0, 1, and 2 mA of current. B) The mean spatial distribution of blink responses during 0, 1, and 2 mA of current, calculated at the peaks of blink deflections. C) Mean and SEM of blink amplitudes at FP1 and FP2 during 0, 1, and 2 mA of applied current. D) Spatial voltage distributions of blink deflections during 1 and 2 mA of current, normalized to 0 mA. Colorbar applies to panel D and E. E) Computational model prediction of the spatial voltage distribution of blink responses during 1 and 2 mA of anodal Bifrontal stimulation. The model prediction supported the presence of blink amplitude increases near the cathode (AF8) and decreases near the anode (AF7). Model scalp voltage in 3D shown for 2 mA of current.

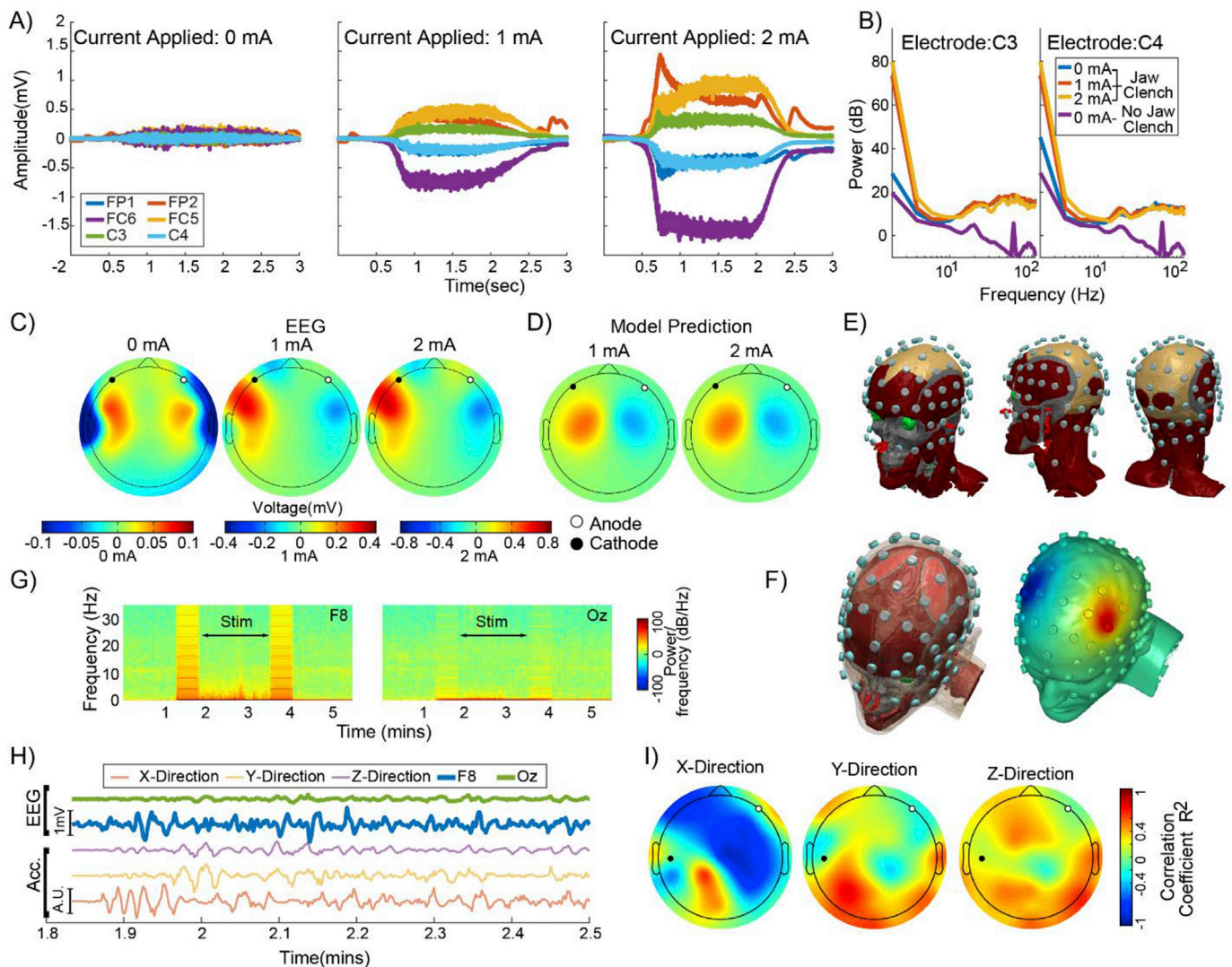


Fig. 8. Myogenic and motion distortion artifacts in EEG during tDCS. A) EMG activity over time, produced by jaw clenches, during the application of 0, 1, and 2 mA of current. Currents were applied with an anodal Bifrontal montage (anode: AF7, cathode: AF8). B) The frequency distribution of bilateral electrodes C3 and C4 comparing EMG activity during 0, 1, 2 mA of stimulation as well as during no stimulation and no EMG activity. C) Average scalp topographies during jaw clenches and 0, 1, and 2 mA of applied current. Colorbars apply to panel C, D, and F. D) Computational model prediction of the spatial scalp distribution of EMG activity resulting from jaw clenches during 1 and 2 mA of stimulation. E) Cephalic muscle groups and underlying tissue of the MRI-derived computational models including the epicranial aponeurosis, occipitalis, masseter, frontalis, and temporalis. F) Area of increased conductivity (left), selected to simulated scalp voltages during muscle activity and its resultant scalp voltage (right, for 2 mA of stimulation). G) Spectrograms at F8 and Oz over the course of pre, during, and post stimulation (2 mA of MISO) with the subject instructed to perform several head movements during stimulation. H) Time-locked EEG and head mounted accelerometry during 2 mA of MISO stimulation and head motion. I) Correlation of accelerometer displacement with EEG voltage distortion over time, over the course of stimulation and head movement.

topographies during 0 mA, highlighted that amplitudes near the anode decreased whereas those near the cathode increased for both 1 and 2 mA (Fig. 7D).

In order to model blink responses, the conductivity of the eyelids was altered during stimulation and the difference between conductivity alterations was taken. The computational model with altered eyelid conductivity was subtracted from the computational model without altered eyelid conductivity. The resultant calculation (Fig. 7E) produced predictions that matched the magnitude and spatial voltage distribution of the EEG (Fig. 7D) and supported the notion that blink amplitudes increased near the cathode (AF8) whereas they decreased near the anode (AF7). Model derived scalp voltage (Fig. 7E) and the normalized blink responses' scalp voltage (Fig. 7D), across current intensities, for anodal Bifrontal stimulation were correlated and the computational model accounted for 79% and 80% of the variance (as indicated by R^2) for 1.0, and 2.0 mA of stimulation, respectively.

3.6. Myogenic and motion distortion artifacts

With stimulation routine 1, high frequency electromyogenic (EMG) or muscle artifacts produced during jaw clenches were examined with the application of anodal Bifrontal stimulation (anode: AF7, cathode: AF8) at intensities of 0, 1, and 2 mA. For 0 mA of applied current or under no stimulation, muscle artifacts produced low amplitude, high frequency interference, typical of EMG signals detected on the scalp. During 1 and 2 mA of current, myogenic activity increased by an offset of ~0.5 and 1.0 mV, respectively, over the course of each muscle contraction (Fig. 8A). The presence of a low frequency offset was highlighted with the removal of the DC voltage by a least-squares linear fit subtraction (Fig. 8A). Additional alterations in the myogenic signal during 2 mA of stimulation were also apparent, namely at the start and end of jaw clenches. In the frequency domain, broadband EMG activity overlapped with frequencies of neural activity, and was most obtrusive above 10 Hz

(Fig. 8B). In addition to differences in power at 0 Hz (DC), between EMG and non EMG conditions, there was a difference in power at higher frequencies (>10 Hz) that extended beyond 100 Hz. Between stimulation conditions (0, 1, 2 mA) though, larger differences in power were present below 10 Hz, suggesting that the effects of DC stimulation during myogenic activity or jaw clenches are confined to lower frequencies (<10 Hz).

In order to compare the spatial distribution of the EMG activity, it was isolated by removing the DC voltage, obtaining the mean voltage across repeated EMG or jaw clench trials and finally computing the mean voltage across the peak myogenic activity over time (Fig. 8C). During 0 mA or no stimulation the spatial distribution of the myogenic activity was centrally located with positive, bilaterally-symmetric dipoles across the scalp. Comparatively, with the application of 1 and 2 mA of current, peak EMG activity was located fronto-centrally with negative and positive dipoles. As current increased from 1 to 2 mA, the area of both dipoles increased and the magnitude approximately doubled (Fig. 8C).

In order to replicate EMG activity resulting from jaw clenches during stimulation, several cephalic muscle groups and underlying tissue were incorporated into MRI-derived computational models including the epicranial aponeurosis, occipitalis, masseter, frontalis, and temporalis (Fig. 8E). Muscle fibers were represented over the mandible for the masseter muscle and over temporal regions of the skull for the temporalis muscles. The scalp voltages produced by stimulation were then computed with either “relaxed” muscle properties (see Methods) assigned or “active” muscle properties. In order to simulate the spatially constrained EMG signal, specific regions of the musculature were selected to have increased conductivity alterations during a simulated contraction (Fig. 8F left). The resultant model prediction for 1 and 2 mA replicated the magnitude of the EMG artifact and approximated the scalp voltage distribution (Fig. 8D). The model predicted increased negative and positive fronto-central activity, similar to the myogenic artifact in EEG; and centralized this activity in close proximity to the temporalis muscles (Fig. 8F right). The computational model derived scalp voltage (Fig. 8D), accounted for 35% and 36% of the variance (as indicated by R^2), for the scalp voltages during jaw clenches with 1 and 2 mA of stimulation (Fig. 8C), respectively.

The motion distortion artifact, induced by slow and rapid head movements under 2 mA for cathodal MISO stimulation, had profound effects on acquired data. In the frequency domain, low frequency broadband distortions were present throughout periods of motion and were exacerbated in electrodes closest to the stimulation sites compared to locations further away (Fig. 8G). EEG data over time with concurrent accelerometry had high degrees of similarities with motion direction during periods of motion (Fig. 8H). Correlations of EEG electrodes and accelerometer deflections corroborated the notion that the distortions seen in EEG channels during head motion were related to the movement of the head and electrodes, which was most likely exacerbated or amplified by the applied DC (Fig. 8I).

4. Discussion

Our overall hypothesis was that inherent physiological artifacts in EEG during tDCS result from stimulation current generating large DC offsets, which are then incrementally modulated by physiology-specific impedances. Physiological artifacts thus take on the temporal characteristics (frequency) of the physiological process while the spatial profile (magnitude) is strongly dictated by both the montage-specific DC offset and physiological change. As such, physiological artifacts are prominent near stimulation electrodes, confounding the detection of “real” neurogenic EEG changes, and the reliance on intensity, polarity, or electrode position experimental controls. Moreover, the DC offset has a slow temporal component (drift) during stimulation (Hahn et al., 2013) and unstable physiological changes, which implies the physiological artifacts may not be as stationary as previously thought. We also report a weak post-stimulation DC offset which suggest the possibility of offline

physiological artifacts, though less pronounced. Confounding efforts to remove noise, these physiological artifacts are inherent (meaning they are present with the use of any device or current source architecture), have a bandwidth specific to physiology (narrowband or broadband in some cases), are larger than neurogenic EEG signals, and exhibit high spatial dimensionality. We discuss the origins of these physiological artifacts, to guide the development of advanced methods that lead to their attenuation. To develop a holistic approach, we also place *inherent physiological artifacts* in the context of more established artifacts we classify as *inherent stimulator artifacts* and *non-inherent artifacts* either *equipment-related* or *physiologic in origin* (Table 1).

In the present study we characterized physiological (current source architecture independent) and demonstrated non-physiological (current source architecture specific) artifacts that arise during concurrent EEG and tDCS. We characterized the voltage and spectral profile of DC stimulation isolating four classes of physiological artifacts, two *inherent*: cardiac distortions, oculomotor distortions; and two *non-inherent*: myogenic distortions, and motion. Each physiological artifact presents a significant and distinct spatiotemporal profile, that can be simulated by physiology-specific computational models.

The most evident EEG artifact during tDCS is the large DC voltages (>100 mV), which were accommodated by the dynamic range (1 V) of our amplifiers for all routines tested. Notably this DC displacement can be three orders magnitude above baseline EEG. For this reason, even an incremental (fraction of a percent) change in DC voltages, as we propose result from physiological changes, can produce relatively large artifacts.

We identified a post stimulation residual voltage, evident up to a minute after stimulation. This was observed across stimulation current source architectures (Fig. 2C), indicating that the residual voltages were independent of stimulator device performance. The magnitude and duration of this post-stimulation voltage may increase with stimulation duration (only short durations were tested with the routines here). It remains an open question to what extent the complex and broadband artifacts identified here during stimulation would manifest during this post-stimulation DC.

4.1. Inherent physiological artifacts

Inherent physiological artifacts can be characterized as being independent of stimulator and EEG hardware and resulting from physiologic modulation of the DC artifact produced by stimulation. When these artifacts cannot be controlled for by experimental design they are ubiquitous and so *inherent*. These include gradual skin impedance changes (DC drift artifacts), cardiac artifacts and oculomotor artifacts.

The DC drift artifacts constitute low frequency voltage changes (DC drift) that occur over the course of stimulation reflecting gradual changes in tissue (skin) impedance (Hahn et al., 2013). With combined tDCS and EEG the DC drift is observed with as little as 60 s of stimulation, can change with stimulation intensity, and can be influenced by ambient and localized stimulation interface temperature (Gholami-Boroujeny et al., 2015). These alterations can be problematic since changes in voltage can occur in orders of magnitude larger than neurogenic signals, whose amplitudes are in turn altered. In terms of artifact removal, overlooking the nonlinear changes in the drifting voltage, can result in poor artifact attenuation and subsequently contaminate data, especially when considering the removal of the cardiac and ocular artifacts.

The cardiac artifact, sometimes referred to as a ballistocardiographic artifact (Rubin and Daube, 2016 Artifacts and the EEG Britton, J; Schmitt, 2017), was observed consistently during stimulation and was highly disruptive to the acquired data. The artifact should not be confused with stimulator generated shifts in voltage (Roy et al., 2014), as it is current source architecture independent (device independent), montage specific, narrowband, and linear with stimulation intensity. The artifact was characterized with a slow rise and fall that was time-locked relative to the R-wave of ECG signals. These traits attested to the artifact changing with blood volume fluctuations, resulting in skin impedance changes during

Table 1
Summary, categorization, and descriptions of different types of EEG artifacts. Artifacts occurring during concurrent tDCS and EEG are placed among artifacts that can occur outside the context of tDCS, as means of providing a holistic perspective of such artifacts. These include inherent stimulator artifacts, inherent physiological artifacts, and non-inherent artifacts, which can be divided into physiological and non-physiological (equipment-related).

| | Inherent Stimulator Artifacts | | | Inherent Physiological Artifacts | | | Non-Inherent Artifacts | | | | |
|----------------------------------|--|--|------------------------------|---|---|---|---|---|--|--|---|
| | Artifacts that are universal, but with varied severity, to any current source architecture, stimulator | | | Independent of current source architecture, stimulator, or EEG system; and result from physiologic integration with “DC” artifact | | | Controllable artifacts that result from non-ideal set-up or experimental conditions | | | | |
| | Broadband Noise Artifact | “On Noise” Artifact | DC-Offset Artifact | DC Drift Artifact | Cardiac Artifact | Blink Artifact | Physiological | | Non-Physiological (Equipment-related) | | |
| Brief Definition | No stimulator can generate ideal DC without some power at unintended frequencies | Leakage or injection of stimulator noise into recording electrodes | DC artifact is no stationary | The non-stationary DC artifact reflects gradual impedance changes by tDCS | May reflect rapid skin impedance change with heart beat that modulates scalp “DC” voltage | May reflect scalp current flow changes resulting from orbit exposure that modulates scalp voltage | Muscle Artifact | Motion Artifact | EEG Saturation | EEG Distortion | Electrode Bridging |
| | No stimulator can generate ideal DC without some power at unintended frequencies | Leakage or injection of stimulator noise into recording electrodes | DC artifact is no stationary | The non-stationary DC artifact reflects gradual impedance changes by tDCS | May reflect rapid skin impedance change with heart beat that modulates scalp “DC” voltage | May reflect scalp current flow changes resulting from orbit exposure that modulates scalp voltage | May reflect change in scalp current flow by muscle conductivity changes | Motion during stimulation can cause “DC” voltage distortions and fluctuations | Theoretically isolated to single channel(s), unless hardware cross talk occurs | Seen if amplifier offset is in a non-linear range or near saturation | Too much gel is applied to EEG/ stimulating electrodes causing false signal recording/ stimulation currents |
| Broadband Changes During Session | Yes | Yes | No | No | No | Yes | Yes | Yes | NA | Yes | Yes |
| Montage Specific | Yes ^a | Yes ^a | Yes ^a | Yes ^a | Yes ^a | Yes ^a | Yes ^a | Yes | Yes | Yes | Yes |
| Outlast Stimulation | No | Possible | Yes | Yes | No | No | No | Possible | Short term. Amplifier carry over possible | No | Yes |
| Additive or Modulatory | Additive | Additive | Additive | Additive | Additive | Additive | Additive | Additive | Additive | Modulatory | Modulatory |

^a Artifact is maximal where skin current density is highest, increases near stimulating electrodes and so is montage (position and current) dependent. Artifact full or partially tracks scalp “DC” voltage (as measured during the experiment and predicted by models) which may be used in correction.

^b Since a function of the “DC” artifact, can change with DC drift or other artifacts that distort the DC directly. Will also change with subjective physiology (e.g. anxiety during tDCS).

stimulation (Noury et al., 2016). For denoising, the concerning aspects of the appearance of the cardiac artifact was its stimulation dependent amplitude, high spatial dimensionality, and time variant scalp distribution. With skin impedance being a dynamic factor, the cardiac artifact could be highly influenced by subjects' physiological and psychological state (Luft and Bhattacharya, 2015), even by anxiety associated with tDCS, which can cause a raise in heart beat and increase sweating, nonlinearly altering acquired data. In electrodes adjacent to stimulation sites, the cardiac artifact was seen to increase up to $\sim 40 \mu\text{V}$ with 2 mA of current, which is much larger than most event related potentials (ERPs; Gebodh et al., 2017; van Dinteren et al., 2014) and raises concerns with previous online concurrent EEG and stimulation studies that have examined ERPs (Cunillera et al., 2016; Faehling and Plewnia, 2016). Changes observed in the overall voltage offset of the ECG signals ($\sim 0.5 \text{ mV}$), measured across the chest during stimulation, also raise further questions about how stimulation interacts with autonomic nervous system (Clancy et al., 2014; Schestatsky et al., 2013b; Schroeder et al., 2015; Vandermeeren et al., 2010), which could in turn result in changes to the cardiac artifact, as well as heart rate or heart rate variability. In the clinical domain, studies examining the online effects of tDCS are cautioned when it comes to patients who have disorders affecting cardiac function. With the aforementioned studies, concurrent ECG with EEG monitoring is highly recommended. As such, patients with cardiac dysfunctions may introduce further variability to the already time variable, oscillating cardiac artifacts, which can be misinterpreted as alterations in low frequency Delta activity.

With concurrent tDCS and EEG, ocular motor distortions, more specifically blink artifacts, were modulated in a montage specific manner. Depending on montage, the blink artifacts' amplitude increased, inverted in polarity, or appeared to be completely attenuated. The amplitude modulation linearly increased or decreased with stimulation intensity, depending on the EEG electrode location relative to stimulation montage. Two potential sources for this were changes in current flow pattern and scalp DC as a result of eyelid closure or polarization of the eyes' corneoretinal dipole (Berg and Scherg, 1991; Iwasaki et al., 2005). Computational models confirmed the first option. Eyelid closure during stimulation altered the path of the applied current on the scalp and distorted the resultant positive amplitude acquired with Cz referential montages. The models explain why near the anode (where a positive scalp voltage was present), blink artifacts had large decreases in amplitude; and conversely near the cathode (where a negative scalp voltage was present), blink artifacts had large increases in voltage during stimulation. These alterations pose problems for automatic artifact rejection algorithms since during stimulation the blink artifact became highly distorted and in some cases undetectable. Left unchecked, blinks can appear as modulations in

low frequency Delta range (0–4 Hz) and be subject dependent. Previous studies examining tDCS effects on blink responses in healthy subjects using EOG (Beyer et al., 2017; Cabib et al., 2016; Zuchowski et al., 2014) may be affected by these artifactual voltage modulations. Similarly, any future studies in the clinical domain using EOG or any combination of tDCS and blink features as online biomarkers with disorders including Parkinson's disease, or multiple sclerosis, would be cautioned. As with other physiological artifacts the use of traditional control experiments (changing montage) and simple signal processing corrections (removal based on fixed threshold detection) may not suffice and multimodal approaches to blink removal/correction are recommended.

4.2. Inherent stimulator artifacts

With concurrent HD-tDCS and EEG, one source of extraphysiological noise introduction are the stimulators themselves. Stimulators that produce variable current outputs, opposed to an ideal constant direct current, will introduce noise in the EEG. These artifacts, referred to as inherent stimulator artifacts, are described as artifacts that are universal to any current source architecture, stimulator, or EEG system used; however, its severity or impact on data quality is variable. Inherent stimulator artifacts can be divided into two main types of artifactual distortions: broadband noise artifact, and “on noise” artifact.

The broadband noise artifact describes the fact that no stimulator or current source architecture can generate an ideal DC without the introduction of power at unintended frequencies. The frequency content of this noise will be device specific and can be broadband including frequencies of physiologic interest with EEG. This type of artifact usually does not outlast stimulation, is montage and current intensity specific having maximal distortion in EEG electrodes nearest to the stimulating electrodes, reflective of the scalp DC voltage.

The “On noise” artifact is the result of any stimulator current manifestation when the device is powered but not applying tDCS. This can result from limitations in device electronics or impedance testing which requires incremental current injection (Fig. 9A). In some cases, large voltage offsets can be seen when the stimulation device is powered on. This type of artifact has been shown to be broadband, montage specific, additive, and can possibly outlast stimulation if the stimulation device is left connected and on.

4.3. Non-inherent artifacts

Artifacts created as a result of non-ideal experimental conditions or set-up can be classified as non-inherent artifacts. This can be divided into non-inherent physiological and non-physiological artifacts. Although

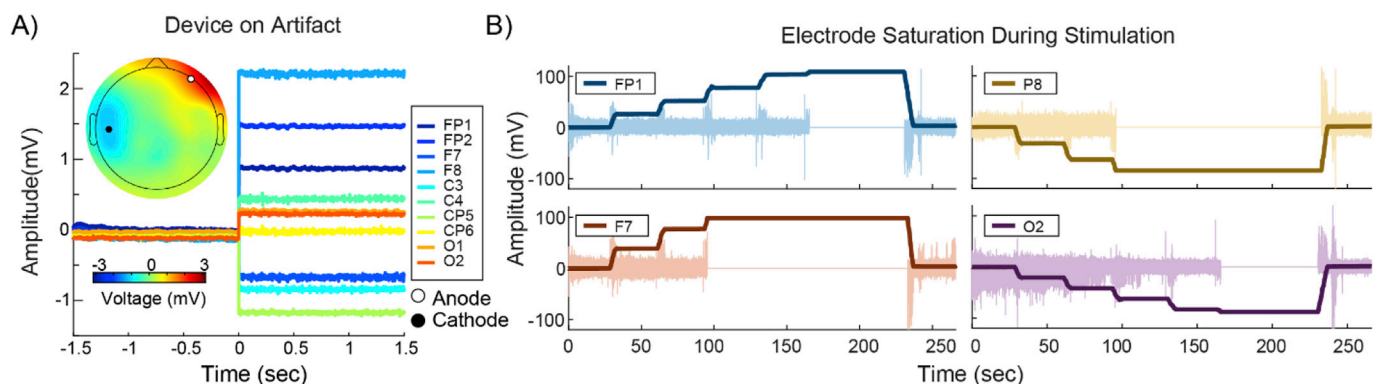


Fig. 9. Device on artifact and saturation of EEG during tDCS. A) Device “On Noise” where time zero onwards indicates when the stimulation device was switched on but not stimulating. Scalp topography is calculated by taking the difference in voltage between device on (after zero) and device off (before zero). B) Electrode saturation over time with gradually increasing current intensity. As current is increased (stepped-up) electrodes (F7 and P8) closest to stimulating sites saturated earlier in time than those further away (FP1 and O2). Darker colors indicate electrode voltage over time whereas lighter colors indicate the derivative of the voltage over time. When the derivative becomes zero, saturation is reached.

non-inherent artifacts span a wide range of sources, here we address physiological: myogenic, motion, and slow-wave drift artifacts, and non-physiological: EEG saturation, EEG distortion, and electrode bridging artifacts.

During stimulation, myogenic artifacts were montage specific, broadband, and modulated in a current intensity specific manner, but like other physiological artifacts presented a unique spatio-temporal profile. Myogenic activity (EMG) is broadband and results from contractions of primarily the epicranial muscles including the masseter, temporalis and frontalis muscles (Goncharova et al., 2003; Whitham et al., 2007). These contractions can significantly contaminate acquired data due to their high amplitude, and broadband spectral and anatomical overlap with neurogenic sources (Barlow, 1985; Shackman et al., 2009). During tDCS this broadband activity was superimposed on a low-frequency shift that increased in magnitude with proximity to stimulation electrodes and with stimulation intensity (Fig. 8A). The muscle activation over time varied as different cephalic muscle groups were engaged. With the activation of different muscle groups during clenching and stimulation, the conductivity of the activated muscles themselves were altered, steering stimulation current, resulting in distinct scalp voltage spatio-temporal patterns. Computational models support (Fig. 8D, E, F) that the low-frequency shift reflects change in muscle impedance and so DC potential, while the superimposed EMG may be unaltered (Fig. 8B).

When combined with stimulation, it becomes increasingly difficult for correction algorithms to reliably separate neurogenic and myogenic sources due to their overlap. These myogenic interactions, like the cardiac artifact, can be influenced by subjects' physiological and psychological state (Bradley et al., 2001; Coan and Allen, 2003; Tassinari et al., 2007; Waterink and van Boxtel, 1994), resulting in teeth grinding, facial muscle tension, eyebrow furrowing etc., leading to variable muscle activation. Even weak facial muscle contractions have been shown to produce low-frequency EEG activity that can be mistaken for changes in cognitive related frequency bands like Alpha rhythms (Goncharova et al., 2003; Lee and Buchsbaum, 1987; Willis et al., 1993). In tDCS this is especially concerning when these artifacts are highly accentuated by stimulation currents. In the clinical setting, these EMG artifacts may appear in patients with conditions including epilepsy, Parkinson's disease, facial myokymia, hemifacial spasm, or palatal myoclonus (Westmoreland, 1996). Caution should be taken in cases like these and other disorders affecting myogenic activity since coupled with stimulation, resultant artifacts can be misinterpreted as epileptiform activity or modulations in the frequency domain.

Movement disruption during EEG and stimulation can result in distortions of neurogenic EEG signals. Abrupt or slow head rotation or tilting can introduce broadband noise. During tDCS even slow neck motions, with displacement in the X, Y and Z, directions from Cz, was associated with disrupted EEG data (Fig. 8G). EEG electrodes near stimulating electrodes (F8) showed the largest distortions over time and frequency whereas those further away (O2) showed lesser distortions supporting the notion that motion artifacts are intensified by presence of large DC potentials. For this reason, caution is warranted even in experiments where subjects are seated and head motion minimized but not fully restricted, as the addition of tDCS may introduce incremental motion artifacts not present in control (no tDCS) conditions, which can be confused for neurogenic changes.

In EEG, slow-wave DC drift artifacts (<0.5 Hz) usually arise from increased perspiration on the scalp (Klass, 1995 American Journal of EEG Technology), which consequently alters skin impedance (Corby et al., 1974; Kappenman and Luck, 2010; Picton and Hillyard, 1972). The addition of tDCS further produced stimulation related scalp impedance changes which taken together changes the DC scalp potentials during tDCS. To the extent that all physiological artifacts identified here resulted from modulations of the scalp DC potentials, then this slow DC drift will contribute to non-stationary physiological artifacts.

As a result of the large DC scalp potentials, tDCS can result in EEG

saturation when the amplifier dynamic range is reached. Increased dynamic range and reduced gain can minimize saturation (Light et al., 2010). For example, in Fig. 9B the amplifier gain was increased, electrodes closest to the anode and cathode (F7 and P8) saturated earlier than those further away (FP1 and O2). When EEG signals approach dynamic range of amplifiers, there is a potential for non-linear signal distortion which would introduce false changes in EEG.

Electrode bridging in EEG often occurs when excessive electrolyte gel is introduced between the scalp and electrodes (Alschuler et al., 2014; Greischar et al., 2004; Tenke and Kayser, 2001). This is a primary reason why HD-tDCS is preferred to sponge saturated or large electrodes. Nonetheless, care must be taken to avoid gel leakage. Electrode bridges during stimulation and EEG can result in current shunting across the scalp, not reaching its proper target, and being introduced directly into the EEG recording electrodes distorting any neurogenic data being acquired.

4.4. Denoising strategies

Currently, there are two general classes of denoising algorithms that can be employed in an attempt to attenuate some stimulation-related artifacts when combining EEG and tDCS: spatial and temporal filtering. Although these classes of algorithms may present some respite from artifact contamination their application is cautioned since they pose risks of degrading the quality of desired signals, artifact amplification as well as unintended artifact introduction. These disadvantages highlight the need for novel, robust artifact removal and attenuation techniques for concurrent EEG and tDCS.

4.4.1. Spatial filtering

The advantage of the spatial filtering approach for artifact removal is that it doesn't require commitment to removal of any specified part of the data's frequency spectrum. Moreover, spatial filtering does not need to be repeated for every individual channel, but is rather performed once on the entire spatiotemporal data record. Spatial filtering is most appropriate when the artifact occupies a subspace of the data, and particularly when that subspace is distinct from the subspace of the desired signal. In the context of combined tDCS-EEG, at least the former certainly holds. The artifact has a spatial distribution that is defined by the montage. Namely, the closer a recording electrode is to an active electrode (anode or cathode), the more likely it is to experience an artifact during stimulation. While it may be argued that the locations near the stimulation electrodes are also the most important for recording, this issue is more nuanced. First, the EEG produced by any single generator is a volume conducted signal that may be picked up across a broad region of the scalp. Second, optimized positions for stimulating a targeted EEG pattern are not necessarily over the maxima of the EEG (Dmochowski et al., 2017). As a result, spatial filtering approaches should be the first line of denoising to be applied to EEG collected during tDCS.

One spatial filtering strategy that may be employed to denoise EEG obtained during tDCS is adaptive noise cancellation (Widrow et al., 1975). The basic idea is to measure a reference noise signal (i.e. a signal dominated by the source of the artifact) and use that signal to regress out any signal components that are correlated with the reference from the recording channels. An intriguing approach here is to utilize the DC signal from the stimulator and DC offset at electrodes as a noise reference, which necessitates not filtering out the DC in hardware, as is performed by many EEG devices. If the DC signal is available, any components of the EEG that fluctuate along with the reference (i.e., are correlated with the noise) can then be identified and removed (Parra et al., 2005). This procedure is similar to the manner in which the EOG artifact is removed in conventional EEG. A disadvantage of this technique is the possibility of artifact amplification. This can occur if artifact dynamics are phase delayed at either the noise reference point or on the scalp, in which case a difference between both would result in a signal with amplified artifact dynamics. This difference can also become

exacerbated with changing scalp impedances over the course of stimulation.

Note that combined tDCS-EEG experiments often employ an EEG-only session where brain activity can be measured prior to the effect of the stimulation. The availability of the EEG not obscured by the tDCS artifact allows for the employment of a powerful spatial filtering approach to denoising, namely Generalized Singular Value Decomposition (GSVD). The basic idea is that two data sets (one corrupted by the stimulation, the other clean) are jointly decomposed into a set of spatial components via the GSVD (Doclo and Moonen, 2002; Golub and Van Loan, 1996). This decomposition yields a set of generalized singular values whose value indicates the relative power of each component in both data records. Components whose power during the stimulation is found to be much stronger are then labeled as artifacts and designated for removal. Denoising is accomplished by reconstructing the data recorded during tDCS but without the contribution of these artifactual sources. The GSVD technique is powerful in that it does not require a noise reference or any knowledge of the artifact. It is most applicable in the case where the source of the artifact occupies a spatial subspace distinct from the desired signal: given that the EEG modulated by stimulation will have a different scalp distribution than the stimulator artifact, the GSVD approach appears to be a viable technique for denoising EEG during tDCS. That being said, our data suggest that tDCS-induced artifacts are high-dimensional due to their spatial non-stationarity; therefore, the removal of these artifacts is likely to significantly distort the desired EEG signal.

4.4.2. Temporal filtering

The fundamental assumption of the temporal filtering approach to denoising is that the artifact can be localized to specific frequency bands and can thus be filtered out of the EEG at each channel. This technique can be effectively utilized if artifact dynamics do not overlap with typical neurogenic frequencies of interest (1–70 Hz). When overlap between neurogenic and artifact sources does occur in the frequency domain, this technique becomes challenging, since determining source-specific portions of spectra with confidence becomes difficult. Some degree of artifact attenuation can be accomplished when neurogenic and artifact sources overlap, however the confidence in reporting artifact-free neural changes is immensely diminished. Temporal filtering also poses the problem of introducing time-domain filtering artifacts (i.e. ringing artifacts) if the appropriate filtering parameters are not applied (Widmann and Schroger, 2012). These time-domain filtering artifacts can be easily overlooked when applied to EEG-tDCS which inherently contains varying degrees of non-linear artifacts. Our data show the presence of narrow-band and broadband artifacts, which were greatly overlapped with neurogenic frequencies, thus the broad application of the temporal filtering technique to EEG-tDCS is greatly cautioned. Temporal filtering may be sufficient in study specific cases where the frequencies of interest can explicitly be shown to reside in ranges clear of inherent physiological activity (possibly >10 Hz), and consists of neurogenic sources of interest.

5. Conclusion

We identified and systematically characterized inherent physiological artifacts during concurrent EEG and High Definition-tDCS (HD-tDCS) including: 1) cardiac distortion; and 2) ocular motor distortion. These physiological artifacts were considered in the context of non-inherent physiological (myogenic and motion distortion artifacts) and non-inherent non-physiological artifacts (equipment-related), as well as inherent stimulator artifacts. Unlike inherent physiological, non-inherent physiological artifacts can, in most cases, be controlled with experimental design- but because they are significantly amplified during tDCS denoising approaches based on baseline EEG (control arm) may fail during stimulation (active arm) leading to spurious results. For example, incremental head or jaw motion may not significantly contaminate control EEG but with online EEG-tDCS these minute changes can introduce detrimental noise, creating artifactual EEG changes.

Typical experimental control arms or correlation of signal with electrode location, do not account for physiological artifacts because of their montage and intensity dependence. Artifacts are high-dimensional, driving the need for improved artifact removal techniques. The attribution of physiological artifacts to DC voltage fluctuations, and leveraging computational models, helps provide a mechanistic substrate to develop and test new signal correction methods. With these improved artifact characterizations more efficient and robust artifact removal techniques can be developed to advance the field and produce more meaningful outcomes.

Conflicts of interest

The City University of New York has patents on Brain Stimulation with MB and LP as inventors. MB and LP have equity in Soterix Medical Inc.

Acknowledgments

This work was supported through (to MB) The City College Fund, and the National Institutes of Health: NIH—NINDS 1R01NS101362, NIH—NIMH 1R01MH111896, NIH—NCI U54CA137788/U54CA132378, and NIH—NIMH 1R01MH109289.

References

- Al-Kaysi, A.M., Al-Ani, A., Loo, C.K., Powell, T.Y., Martin, D.M., Breakspear, M., Boonstra, T.W., 2017. Predicting tDCS treatment outcomes of patients with major depressive disorder using automated EEG classification. *J. Affect. Disord.* 208, 597–603.
- Alschuler, D.M., Tenke, C.E., Bruder, G.E., Kayser, J., 2014. Identifying electrode bridging from electrical distance distributions: a survey of publicly-available EEG data using a new method. *Clin. Neurophysiol.* 125, 484–490.
- Antal, A., Bikson, M., Datta, A., Lafon, B., Dechent, P., Parra, L.C., Paulus, W., 2014. Imaging artifacts induced by electrical stimulation during conventional fMRI of the brain. *Neuroimage* 85.
- Barlow, J.S., 1985. A general-purpose automatic multichannel electronic switch for EEG artifact elimination. *Electroencephalogr. Clin. Neurophysiol.* 60, 174–176.
- Baudewig, J., Nitsche, M.A., Paulus, W., Frahm, J., 2001. Regional modulation of BOLD MRI responses to human sensorimotor activation by transcranial direct current stimulation. *Magn. Reson. Med.* 45, 196–201.
- Baudewig, J., Siebner, H.R., Bestmann, S., Tergau, F., Tings, T., Paulus, W., Frahm, J., 2018. Functional MRI of cortical activations induced by transcranial magnetic stimulation (tms). *Neuroreport* 12, 3543–3548.
- Berg, P., Scherg, M., 1991. Dipole models of eye movements and blinks. *Electroencephalogr. Clin. Neurophysiol.* 79, 36–44.
- Beyer, L., Batsikadze, G., Timmann, D., Gerwig, M., 2017. Cerebellar tDCS effects on conditioned eyeblinks using different electrode placements and stimulation protocols. *Front. Hum. Neurosci.* 11, 23.
- Bikson, M., Rahman, A., Datta, A., 2012. Computational models of transcranial direct current stimulation. *Clin. EEG Neurosci.* 43, 176–183.
- Bradley, M.M., Codispoti, M., Cuthbert, B.N., Lang, P.J., 2001. Emotion and motivation I: defensive and appetitive reactions in picture processing. *Emotion* 1, 276–298.
- Brunoni, A.R., Nitsche, M.A., Bolognini, N., Bikson, M., Wagner, T., Merabet, L., Edwards, D.J., Valero-Cabre, A., Rotenberg, A., Pascual-Leone, A., Ferrucci, R., Priori, A., Boggio, P.S., Fregni, F., 2012. Clinical research with transcranial direct current stimulation (tDCS): challenges and future directions. *Brain Stimul* 5, 175–195.
- Buch, E.R., Santarnecchi, E., Antal, A., Born, J., Celnik, P.A., Classen, J., Gerloff, C., Hallett, M., Hummel, F.C., Nitsche, M.A., Pascual-Leone, A., Paulus, W.J., Reis, J., Robertson, E.M., Rothwell, J.C., Sandrini, M., Schambra, H.M., Wassermann, E.M., Ziemann, U., Cohen, L.G., 2017. Effects of tDCS on motor learning and memory formation: a consensus and critical position paper. *Clin. Neurophysiol.* 128, 589–603.
- Cabib, C., Cipullo, F., Morales, M., Valls-Sole, J., 2016. Transcranial direct current stimulation (tDCS) enhances the excitability of trigemino-facial reflex circuits. *Brain Stimul* 9, 218–224.
- Cancelli, A., Cottone, C., Tecchio, F., Truong, D.Q., Dmochowski, J., Bikson, M., 2016. A simple method for EEG guided transcranial electrical stimulation without models. *J. Neural. Eng.* 13, 036022.
- Castillo-Saavedra, L., Gebodh, N., Bikson, M., Diaz-Cruz, C., Brandao, R., Coutinho, L., Truong, D., Datta, A., Shani-Hershkovich, R., Weiss, M., Lauffer, I., Reches, A., Peremen, Z., Geva, A., Parra, L.C., Fregni, F., 2016. Clinically effective treatment of fibromyalgia pain with high-definition transcranial direct current stimulation: phase II open-label dose optimization. *J. Pain* 17, 14–26.
- Charvet, L.E., Kasschau, M., Datta, A., Knotkova, H., Stevens, M.C., Alonzo, A., Loo, C., Krull, K.R., Bikson, M., 2015. Remotely-supervised transcranial direct current stimulation (tDCS) for clinical trials: guidelines for technology and protocols. *Front. Syst. Neurosci.* 9, 26.

- Chung, S.W., Rogasch, N.C., Hoy, K.E., Fitzgerald, P.B., 2015. Measuring brain stimulation induced changes in cortical properties using TMS-EEG. *Brain Stimul* 8, 1010–1020.
- Clancy, J.A., Johnson, R., Raw, R., Deuchars, S.A., Deuchars, J., 2014. Anodal transcranial direct current stimulation (tDCS) over the motor cortex increases sympathetic nerve activity. *Brain Stimul* 7, 97–104.
- Coan, J.A., Allen, J.J., 2003. Varieties of emotional experience during voluntary emotional facial expressions. *Ann. N. Y. Acad. Sci.* 1000, 375–379.
- Corby, J.C., Roth, W.T., Kopell, B.S., 1974. Prevalence and methods of control of the cephalic skin potential EEG artifact. *Psychophysiology* 11, 350–360.
- Cunillera, T., Brignani, D., Cucurell, D., Fuentesmilla, L., Miniussi, C., 2016. The right inferior frontal cortex in response inhibition: a tDCS-ERP co-registration study. *Neuroimage* 140, 66–75.
- Datta, A., Bansal, V., Diaz, J., Patel, J., Reato, D., Bikson, M., 2009. Gyri-precise head model of transcranial direct current stimulation: improved spatial focality using a ring electrode versus conventional rectangular pad. *Brain Stimul* 2, 201–207, 207 e201.
- Datta, A., Zhou, X., Su, Y., Parra, L.C., Bikson, M., 2013. Validation of finite element model of transcranial electrical stimulation using scalp potentials: implications for clinical dose. *J. Neural. Eng.* 10, 036018.
- Delorme, A., Makeig, S., 2004. EEGLAB: an open source toolbox for analysis of single-trial EEG dynamics including independent component analysis. *J. Neurosci. Methods* 134, 9–21.
- Dmochowski, J.P., Koessler, L., Norcia, A.M., Bikson, M., Parra, L.C., 2017. Optimal use of EEG recordings to target active brain areas with transcranial electrical stimulation. *Neuroimage* 157, 69–80.
- Doclo, S., Moonen, M., 2002. GSVD-based optimal filtering for single and multimicrophone speech enhancement. *IEEE Trans. Signal Process.* 50, 2230–2244.
- Eyuboglu, B.M., Brown, B.H., Barber, D.C., 1989. In vivo imaging of cardiac related impedance changes. *IEEE Eng. Med. Biol. Mag.* 8, 39–45.
- Faehling, F., Plewnia, C., 2016. Controlling the emotional bias: performance, late positive potentials, and the effect of anodal transcranial direct current stimulation (tDCS). *Front. Cell. Neurosci.* 10, 159.
- Faria, P., Fregni, F., Sebastiao, F., Dias, A.I., Leal, A., 2012. Feasibility of focal transcranial DC polarization with simultaneous EEG recording: preliminary assessment in healthy subjects and human epilepsy. *Epilepsy Behav.* 25, 417–425.
- Fernandez-Corazza, M., Turovets, S., Luu, P., Anderson, E., Tucker, D., 2016. Transcranial electrical neuromodulation based on the reciprocity principle. *Front. Psychiatr.* 7, 87.
- Garcia-Cossio, E., Witkowski, M., Robinson, S.E., Cohen, L.G., Birbaumer, N., Soekadar, S.R., 2016. Simultaneous transcranial direct current stimulation (tDCS) and whole-head magnetoencephalography (MEG): assessing the impact of tDCS on slow cortical magnetic fields. *Neuroimage* 140, 33–40.
- Gebodh, N., Vanegas, M.I., Kelly, S.P., 2017. Effects of stimulus size and contrast on the initial primary visual cortical response in humans. *Brain Topogr.* 30, 450–460.
- Gholami-Boroujeni, S., Mekonnen, A., Batkin, I., Bolic, M., 2015. Theoretical analysis of the effect of temperature on current delivery to the brain during tDCS. *Brain Stimul* 8, 509–514.
- Golub, G.H., Van Loan, C.F., 1996. *Matrix Computations*, third ed. Johns Hopkins University Press.
- Goncharova, I.I., McFarland, D.J., Vaughan, T.M., Wolpaw, J.R., 2003. EMG contamination of EEG: spectral and topographical characteristics. *Clin. Neurophysiol.* 114, 1580–1593.
- Greischar, L.L., Burghy, C.A., van Reekum, C.M., Jackson, D.C., Pizzagalli, D.A., Mueller, C., Davidson, R.J., 2004. Effects of electrode density and electrolyte spreading in dense array electroencephalographic recording. *Clin. Neurophysiol.* 115, 710–720.
- Hahn, C., Rice, J., Macuff, S., Minhas, P., Rahman, A., Bikson, M., 2013. Methods for extra-low voltage transcranial direct current stimulation: current and time dependent impedance decreases. *Clin. Neurophysiol.* 124, 551–556.
- Huang, Y., Dmochowski, J.P., Su, Y., Datta, A., Rorden, C., Parra, L.C., 2013. Automated MRI segmentation for individualized modeling of current flow in the human head. *J. Neural. Eng.* 10.
- Huang, Y., Liu, A.A., Lafon, B., Friedman, D., Dayan, M., Wang, X., Bikson, M., Doyle, W.K., Devinsky, O., Parra, L.C., 2017. Measurements and models of electric fields in the in vivo human brain during transcranial electric stimulation. *eLife* 6, e18834. <https://doi.org/10.7554/eLife.18834>.
- Hunter, M.A., Coffman, B.A., Trumbo, M.C., Clark, V.P., 2013. Tracking the neuroplastic changes associated with transcranial direct current stimulation: a push for multimodal imaging. *Front. Hum. Neurosci.* 7, 495.
- Iwasaki, M., Kellinghaus, C., Alexopoulos, A.V., Burgess, R.C., Kumar, A.N., Han, Y.H., Luders, H.O., Leigh, R.J., 2005. Effects of eyelid closure, blinks, and eye movements on the electroencephalogram. *Clin. Neurophysiol.* 116, 878–885.
- Kappenman, E.S., Luck, S.J., 2010. The effects of electrode impedance on data quality and statistical significance in ERP recordings. *Psychophysiology* 47, 888–904.
- Klass, D.W., 1995. The continuing challenge of artifacts in the EEG. *Am. J. EEG Technol.* 35, 239–269.
- Komssi, S., Aronen, H.J., Huttunen, J., Kesaniemi, M., Soinnie, L., Nikouline, V.V., Ollikainen, M., Roine, R.O., Karhu, J., Savolainen, S., Ilmoniemi, R.J., 2002. Ipsi- and contralateral EEG reactions to transcranial magnetic stimulation. *Clin. Neurophysiol.* 113, 175–184.
- Lee, S., Buchsbaum, M.S., 1987. Topographic mapping of EEG artifacts. *Clin. Electroencephalogr.* 18, 61–67.
- Li, L., Shin, H., Li, X., Li, S., Zhou, P., 2016. Localized electrical impedance myography of the biceps brachii muscle during different levels of isometric contraction and fatigue. *Sensors* 16.
- Light, G.A., Williams, L.E., Minow, F., Sprock, J., Rissling, A., Sharp, R., Swerdlow, N.R., Braff, D.L., 2010. Electroencephalography (EEG) and event-related potentials (ERPs) with human participants. *Curr. Protoc. Neurosci.* Chapter 6, 21–24. Unit 6.25.
- Luft, C.D., Bhattacharya, J., 2015. Aroused with heart: modulation of heartbeat evoked potential by arousal induction and its oscillatory correlates. *Sci. Rep.* 5, 15717.
- Mancini, M., Pellicciari, M.C., Brignani, D., Mauri, P., De Marchis, C., Miniussi, C., Conforto, S., 2015. Automatic artifact suppression in simultaneous tDCS-EEG using adaptive filtering. *Conf. Proc. IEEE Eng. Med. Biol. Soc.* 2015, 2729–2732.
- Mangia, A.L., Pirini, M., Cappello, A., 2014. Transcranial direct current stimulation and power spectral parameters: a tDCS/EEG co-registration study. *Front. Hum. Neurosci.* 8, 601.
- Minhas, P., Bansal, V., Patel, J., Ho, J.S., Diaz, J., Datta, A., Bikson, M., 2010. Electrodes for high-definition transcutaneous DC stimulation for applications in drug delivery and electrotherapy, including tDCS. *J. Neurosci. Methods* 190, 188–197.
- Ngai, S.P., Jones, A.Y., 2013. Changes in skin impedance and heart rate variability with application of Acu-TENS to BL 13 (Feishu). *J. Alternative Compl. Med.* 19, 558–563.
- Noury, N., Hipp, J.F., Siegel, M., 2016. Physiological processes non-linearly affect electrophysiological recordings during transcranial electric stimulation. *Neuroimage* 140, 99–109.
- Parra, L.C., Spence, C.D., Gerson, A.D., Sajda, P., 2005. Recipes for the linear analysis of EEG. *Neuroimage* 28, 326–341.
- Picton, T.W., Hillyard, S.A., 1972. Cephalic skin potentials in electroencephalography. *Electroencephalogr. Clin. Neurophysiol.* 33, 419–424.
- Roy, A., Baxter, B., He, B., 2014. High-definition transcranial direct current stimulation induces both acute and persistent changes in broadband cortical synchronization: a simultaneous tDCS-EEG study. *IEEE Trans. Biomed. Eng.* 61, 1967–1978.
- Rubin, D., Daube, J., 2016. *Adult EEG: Artifacts and the EEG*. Clinical Neurophysiology. Oxford University Press.
- Salimpour, Y., Wei, Z., Duy, P.Q., Anderson, W.S., 2016. Does transcranial direct current stimulation actually deliver DC stimulation? *Brain Stimul* 9, 623–624.
- Schestsatsky, P., Morales-Quezada, L., Fregni, F., 2013a. Simultaneous EEG monitoring during transcranial direct current stimulation. *J. Vis. Exp.* (76), e50426 <https://doi.org/10.3791/50426>.
- Schestsatsky, P., Simis, M., Freeman, R., Pascual-Leone, A., Fregni, F., 2013b. Non-invasive brain stimulation and the autonomic nervous system. *Clin. Neurophysiol.* 124, 1716–1728.
- Schmitt, S., 2017. Artifacts resembling seizures. In: Husain, A.M., Sinha, S.R. (Eds.), *Continuous EEG Monitoring: Principles and Practice*. Springer International Publishing, Cham, pp. 153–171.
- Schroeder, P.A., Ehlis, A.C., Wolkenstein, L., Fallgatter, A.J., Plewnia, C., 2015. Emotional distraction and bodily reaction: modulation of autonomous responses by anodal tDCS to the prefrontal cortex. *Front. Cell. Neurosci.* 9, 482.
- Shackman, A.J., McMenamin, B.W., Slatger, H.A., Maxwell, J.S., Greischar, L.L., Davidson, R.J., 2009. Electromyogenic artifacts and electroencephalographic inferences. *Brain Topogr.* 22, 7–12.
- Shiffman, C.A., Aaron, R., Rutkove, S.B., 2003. Electrical impedance of muscle during isometric contraction. *Physiol. Meas.* 24, 213–234.
- Tassinary, L.G., Cacioppo, J.T., Vanman, E.J., 2007. The skeletomotor system. In: Berntson, G., Cacioppo, J.T., Tassinary, L.G. (Eds.), *Handbook of Psychophysiology*. Cambridge University Press, Cambridge, pp. 267–300.
- Tenke, C.E., Kayser, J., 2001. A convenient method for detecting electrolyte bridges in multichannel electroencephalogram and event-related potential recordings. *Clin. Neurophysiol.* 112, 545–550.
- van Dinteren, R., Arns, M., Jongsma, M.L., Kessels, R.P., 2014. P300 development across the lifespan: a systematic review and meta-analysis. *PLoS One* 9, e87347.
- Vandermeeren, Y., Jamart, J., Ossemann, M., 2010. Effect of tDCS with an extracephalic reference electrode on cardio-respiratory and autonomic functions. *BMC Neurosci.* 11, 38.
- Villamar, M.F., Volz, M.S., Bikson, M., Datta, A., Dasilva, A.F., Fregni, F., 2013. Technique and considerations in the use of 4x1 ring high-definition transcranial direct current stimulation (HD-tDCS). *JoVE*, e50309.
- Wagner, S., Lucka, F., Vorwerk, J., Herrmann, C.S., Nolte, G., Burger, M., Wolters, C.H., 2016. Using reciprocity for relating the simulation of transcranial current stimulation to the EEG forward problem. *Neuroimage* 140, 163–173.
- Waterink, W., van Boxtel, A., 1994. Facial and jaw-elevator EMG activity in relation to changes in performance level during a sustained information processing task. *Biol. Psychol.* 37, 183–198.
- Westmoreland, B.F., 1996. Periodic patterns in the EEG. *Am. J. Electroencephalogr. Technol.* 36, 1–17.
- Whitham, E.M., Pope, K.J., Fitzgibbon, S.P., Lewis, T., Clark, C.R., Loveless, S., Broberg, M., Wallace, A., DeLosAngeles, D., Lillie, P., Hardy, A., Franks, R., Pulbrook, A., Willoughby, J.O., 2007. Scalp electrical recording during paralysis: quantitative evidence that EEG frequencies above 20 Hz are contaminated by EMG. *Clin. Neurophysiol.* 118, 1877–1888.
- Widmann, A., Schroger, E., 2012. Filter effects and filter artifacts in the analysis of electrophysiological data. *Front. Psychol.* 3, 233.
- Widrow, B., Glover, J.R., McCool, J.M., Kaunitz, J., Williams, C.S., Hearn, R.H., Zeidler, J.R., Dong, J.E., Goodlin, R.C., 1975. Adaptive noise cancelling: principles and applications. *Proc. IEEE* 63, 1692–1716.
- Willis, J., Nelson, A., Rice, J., Black, F.W., 1993. The topography of muscle activity in quantitative EEG. *Clin. Electroencephalogr.* 24, 123–126.
- Zuchowski, M.L., Timmann, D., Gerwig, M., 2014. Acquisition of conditioned eyeblink responses is modulated by cerebellar tDCS. *Brain Stimul* 7, 525–531.